

Boise State University

ScholarWorks

Geosciences Faculty Publications and
Presentations

Department of Geosciences

9-2022

Relative Timing of Off-Axis Volcanism from Sediment Thickness Estimates on the 8°20'N Seamount Chain, East Pacific Rise

Andrea Fabbrizzi
San Diego State University

Ross Parnell-Turner
Scripps Institution of Oceanography

Patricia M. Gregg
University of Illinois at Urbana-Champaign

Daniel J. Fornari
Woods Hole Oceanographic Institution

Michael R. Perfit
University of Florida

See next page for additional authors

—

Authors

Andrea Fabbrizzi, Ross Parnell-Turner, Patricia M. Gregg, Daniel J. Fornari, Michael R. Perfit, V. Dorsey Wanless, and Molly Anderson

Geochemistry, Geophysics, Geosystems®



RESEARCH ARTICLE

10.1029/2022GC010335

Key Points:

- Regional bathymetry and near-bottom sonar surveys investigate the structure and history of the 8°20'N seamount chain, west of the East Pacific Rise (EPR)
- Sediment thickness from autonomous underwater vehicle subbottom compressed high-intensity radiated pulse images are used to estimate the relative age of magmatism at nine seamounts along chain
- Sediment thickness does not increase with distance from the EPR axis, implying that magmatism was episodic and prolonged

Supporting Information:

Supporting Information may be found in the online version of this article.

Correspondence to:

A. Fabbrizzi,
afabbriz@ucsd.edu

Citation:

Fabbrizzi, A., Parnell-Turner, R., Gregg, P. M., Fornari, D. J., Perfit, M. R., Wanless, V. D., & Anderson, M. (2022). Relative timing of off-axis volcanism from sediment thickness estimates on the 8°20'N seamount chain, East Pacific Rise. *Geochemistry, Geophysics, Geosystems*, 23, e2022GC010335. <https://doi.org/10.1029/2022GC010335>

Received 13 JAN 2022
Accepted 20 JUL 2022






Author Contributions:

Conceptualization: Andrea Fabbrizzi, Ross Parnell-Turner, Patricia M. Gregg, Daniel J. Fornari, Michael R. Perfit, V. Dorsey Wanless, Molly Anderson

Data curation: Andrea Fabbrizzi, Ross Parnell-Turner

Formal analysis: Andrea Fabbrizzi, Ross Parnell-Turner, Daniel J. Fornari

Relative Timing of Off-Axis Volcanism From Sediment Thickness Estimates on the 8°20'N Seamount Chain, East Pacific Rise

Andrea Fabbrizzi^{1,2} , Ross Parnell-Turner² , Patricia M. Gregg³, Daniel J. Fornari⁴ , Michael R. Perfit⁵ , V. Dorsey Wanless⁶ , and Molly Anderson⁵

¹Department of Geological Sciences, San Diego State University, San Diego, CA, USA, ²Scripps Institution of Oceanography, University of California, San Diego, La Jolla, CA, USA, ³Department of Geology, University of Illinois at Urbana-Champaign, Urbana, IL, USA, ⁴Department of Geology and Geophysics, Woods Hole Oceanographic Institution, Woods Hole, MA, USA, ⁵Department of Geological Sciences, University of Florida, Gainesville, FL, USA, ⁶Department of Geosciences, Boise State University, Boise, ID, USA

Abstract Volcanic seamount chains on the flanks of mid-ocean ridges record variability in magmatic processes associated with mantle melting over several millions of years. However, the relative timing of magmatism on individual seamounts along a chain can be difficult to estimate without *in situ* sampling and is further hampered by Ar⁴⁰/Ar³⁹ dating limitations. The 8°20'N seamount chain extends ~170 km west from the fast-spreading East Pacific Rise (EPR), north of and parallel to the western Siqueiros fracture zone. Here, we use multibeam bathymetric data to investigate relationships between abyssal hill formation and seamount volcanism, transform fault slip, and tectonic rotation. Near-bottom compressed high-intensity radiated pulse, bathymetric, and sidescan sonar data collected with the autonomous underwater vehicle *Sentry* are used to test the hypothesis that seamount volcanism is age-progressive along the seamount chain. Although sediment on seamount flanks is likely to be reworked by gravitational mass-wasting and current activity, bathymetric relief and *Sentry* vehicle heading analysis suggest that sedimentary accumulations on seamount summits are likely to be relatively pristine. Sediment thickness on the seamounts' summits does not increase linearly with nominal crustal age, as would be predicted if seamounts were constructed proximal to the EPR axis and then aged as the lithosphere cooled and subsided away from the ridge. The thickest sediments are found at the center of the chain, implying the most ancient volcanism there, rather than on seamounts furthest from the EPR. The nonlinear sediment thickness along the 8°20'N seamounts suggests that volcanism can persist off-axis for several million years.

Plain Language Summary Most of the volcanism on Earth happens in the oceans, at mid-ocean ridges where plates spread apart. In some places, however, chains of volcanoes that extend over distances of hundreds of kilometers long can form away from the ridge axis. The formation of these volcanic chains, called off-axis seamounts, is poorly understood, yet understanding their origins will help learn about processes taking place deep inside Earth's mantle. We used a sonar carried by an underwater robot in water depths of ~3 km to measure the thickness of sedimentary mud on top of a seamount chain in the eastern Pacific Ocean at 8°20'N. The thicker the sediment, the greater the time that has passed since the last volcanic eruption. We found that sediments do not simply thicken with seafloor age, implying that volcanoes in these types of seamount chains can remain active over millions of years.

1. Introduction

Although the early discovery of volcanism on mid-ocean ridges (MORs) made a major contribution to the development of modern plate tectonic theory, debate has continued about the spatial and temporal relationships between near- and off-axis volcanism associated with MOR magmatism (Ballmer et al., 2013; Niu & Batiza, 1997; Perfit et al., 1994; Reynolds & Langmuir, 2000; Sohn & Sims, 2005; Waters et al., 2013). The distribution and shape of seamounts provide important information on the timing of intraplate and spreading-center related volcanism and crustal and mantle melting processes, as seamounts have the potential to sample both the on- and off-axis melt regimes (Batiza, 1982; Smith, 1988; Toomey et al., 2007). At MORs, seamounts proximal to the axis are often small, ~<1 km in relief, and are located in a variety of settings. These include groups or lineaments near

© 2022. American Geophysical Union.
All Rights Reserved.
This is an open access article under the terms of the [Creative Commons Attribution License](https://creativecommons.org/licenses/by/4.0/), which permits use, distribution and reproduction in any medium, provided the original work is properly cited.

Funding acquisition: Patricia M. Gregg, Daniel J. Fornari, Michael R. Perfit, V. Dorsey Wanless

transform faults and fracture zones, associated with overlapping spreading centers (OSCs), and over regions of anomalously high magma supply (Batiza, 1982; Fornari, Perfit, Allan, & Batiza, 1988; Hillier & Watts, 2007; Smith & Cann, 1992). Volcanism at fast-spreading MORs is thought to be limited to crustal ages of 0.1–0.2 Ma (Alexander & Macdonald, 1996; White et al., 1998), or within ~10 km of the spreading center since melt is expected to be focused toward the axis (Katz et al., 2006). In addition to the primary melt supply, tectonic deformation, plate spreading rate, spreading asymmetry, small changes in relative motion, as well as the composition of source melt(s), are all likely to impact the distribution and morphology of near-axis seamounts (Clague et al., 2000; Coumans et al., 2014; Davis & Karsten, 1986; Langmuir et al., 1992).

Compared to on-axis regions, our understanding of off-axis volcanic systems is largely based upon dredging and infrequent submersible dive programs that have sampled and compiled petrologic and geochemical observations of near-axis seamounts and ridge flanks (Batiza & Vanko, 1984; Clague et al., 2000; Davis & Clague, 2000; Fornari, Perfit, Allan, & Batiza, 1988; Fornari, Perfit, Allan, Batiza, Haymon et al., 1988; Macdonald et al., 1992). Off-axis seamounts offer the possibility of a window into mantle processes, since they form away from the homogenizing effect of a steady-state magma chamber (Batiza & Niu, 1992), and are usually less influenced by the tectonic interaction between a MOR and slip on active transform faults (Pockalny et al., 1997). However, a few cases of intraplate volcanism, such as between 13°40'S and 14°15'S on the East Pacific Rise (EPR), suggest that seamount chains may be related to axial magma plumbing, even though they can extend ~70 km from the axis (White, Umino, & Kumagai, 2006). Some isolated near-axis seamounts are attributed to magma chambers associated with mantle upwelling close to the MOR (Harmon et al., 2011; Scheirer & Macdonald, 1995), while further off-axis, isolated seamounts, and short chains of seamounts, are thought to form due to the presence of mantle heterogeneities that deliver melt to the crust without influence from the wide zone of decompression melting proposed to occur beneath MORs (Anderson et al., 2021; Davis & Karsten, 1986; Fornari, Perfit, Allan, & Batiza, 1988).

To understand the processes controlling seamount formation, it is necessary to place temporal constraints on magmatism during emplacement and growth. Since in situ samples of fresh basaltic rocks from volcanic constructs on the seafloor are difficult to obtain and their geochemical characteristics (i.e., low potassium contents) render them difficult to date by routine dating techniques, only a handful of seamounts have been radiometrically dated (Briais et al., 2009; Clouard & Bonneville, 2005; Koppers et al., 2004, 2012). In order to overcome this problem, indirect estimates of seamount age have been obtained by modeling the flexural response of the lithospheric plate to a volcanic load or by analyzing magnetic anomaly profiles (Choi et al., 2021; Hwang & Kim, 2016; Watts et al., 1988, 2006). Here, we use an alternative approach, based on the thickness of sediment accumulated on top of newly formed seamounts, which is a novel proxy for the relative timing of seamount construction along linear chains located on the flanks of a MOR.

We quantify the relative timing of volcanism along the 8°20'N seamount chain, which extends ~170 km away from the fast-spreading EPR, using near-bottom data collected by autonomous underwater vehicle (AUV) *Sentry* and human-occupied vehicle (HOV) *Alvin*. Sediment thickness estimates from compressed high-intensity radiated pulse (CHIRP) images are used as a proxy for relative ages of the underlying seamount crust in combination with near-bottom bathymetric, side-scan sonar, and photographic data to constrain the relative timing of volcanism. These observations are then used to test two alternate hypotheses: (a) that volcanic constructs along the 8°20'N seamount chain are linearly age-progressive, with volcanic activity and growth restricted to within a few kilometers of the EPR axis, and then passively spread westward; or (b) off-axis seamounts west of the EPR axis are not age-progressive, and were emplaced at variable distances off-axis over millions of years. This approach can provide a better understanding of mantle melting and submarine volcanic processes that create oceanic lithosphere at a fast-spreading MOR.

1.1. Study Area: 8°20'N Seamount Chain

Between 8° and 11°N, the EPR spreads at a full rate of ~107 mm/yr (Carbotte & Macdonald, 1992; DeMets et al., 2010), and is divided into several first- and lower-order segments by large-offset transform faults, OSCs and smaller deviations of axial linearity (also known as DEVALS; Langmuir et al., 1986; White, Haymon, & Carbotte, 2006). These offsets in the linearity of the EPR axis have been shown to be related to discontinuities and variability in the underlying axial melt lens (Carbotte et al., 2013; Haymon et al., 1991; Lonsdale, 1993; Macdonald et al., 1988). Near 8°20'N, the EPR is offset by 140 km in a left-lateral sense by the Siqueiros

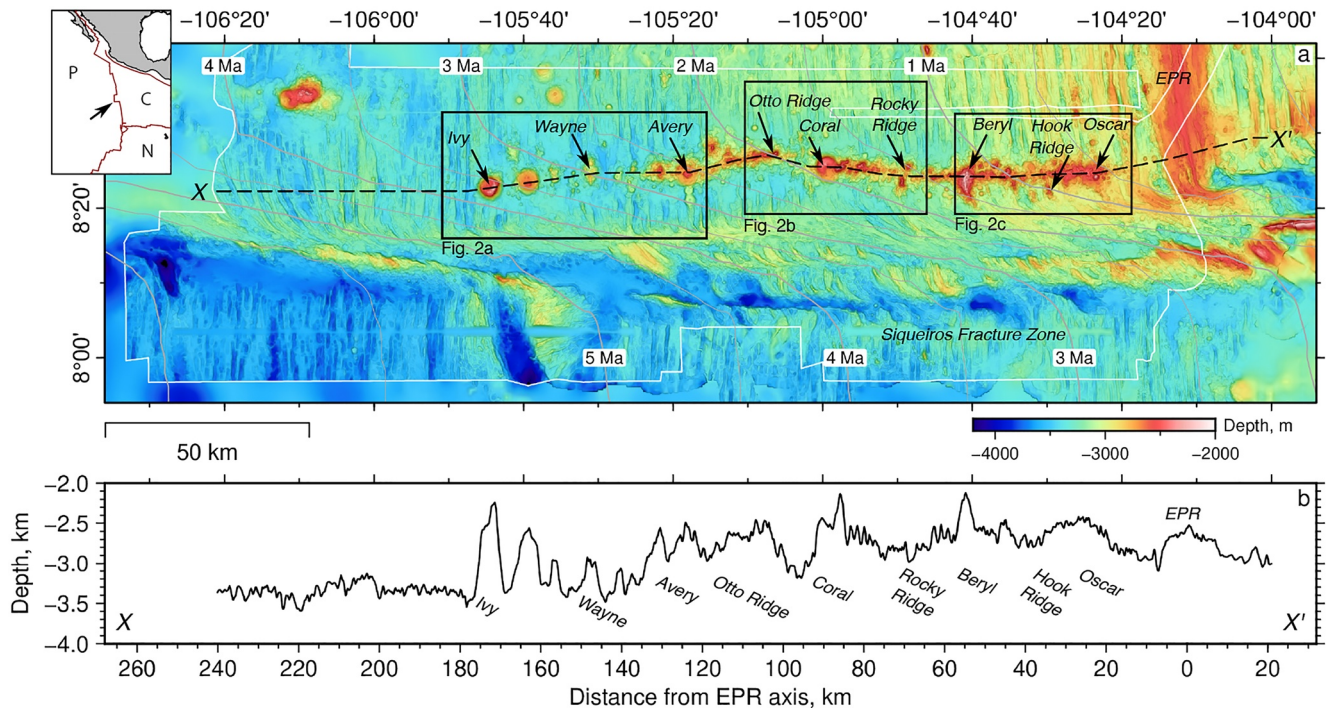


Figure 1. (a) Multibeam bathymetric map of the 8°20'N seamount chain, western Siqueiros fracture zone and western flank of the East Pacific Rise, acquired on RV *Atlantis* cruise AT37-05 in 2016. Boxes show locations of panels in Figure 2; thin white line is extent of 2016 multibeam bathymetric survey; gray lines are crustal isochrons (Seton et al., 2020); black-dashed line is profile X-X' plotted in (b). Inset: red lines are plate boundaries; P, C, and N are Pacific, Cocos, and Nazca plates, respectively; arrow indicates study site. (b) Bathymetric profile X-X', with seamount positions noted.

transform, which itself is a ~20 km-wide deformation zone (Crane, 1976), containing several intratransform spreading centers (Fornari et al., 1989). West of the EPR axis and on the northern side of the Siqueiros fracture zone trace near 8°20'N, is a chain of volcanoes and constructional ridges consisting of coalesced seamounts (Figure 1). The eastern end of the chain is located ~30 km northwest of the western ridge-transform intersection of the Siqueiros transform with the EPR. The main trend of volcanoes and coalesced volcanic ridges that comprise the chain lie ~20 km north of, and nearly parallel to, the western Siqueiros fracture zone (Behn et al., 2002; Carbotte & Macdonald, 1992; Scheirer & Macdonald, 1995).

At a regional scale, the seamounts follow a trend of ~260°, while other seamount groups or chains along that section of the EPR, most notably the Lamont Seamounts to the north (Allan et al., 1989; Fornari, Perfit, Allan, & Batiza, 1988; Fornari, Perfit, Allan, Batiza, Haymon et al., 1988), are aligned parallel to the absolute motion trend of ~330°. The presence of intratransform spreading centers in the Siqueiros transform (Fornari et al., 1989; Gregg et al., 2009; Hebert & Montési, 2011; Perfit et al., 1996) and the evolution and reorganization of the plate boundary in this area (Pockalny et al., 1997) over the past few million years has resulted in several generally east-west trending structural lineaments on the Cocos plate that juxtapose the 8°20'N seamounts west of the EPR axis. These features are probably relicts of the northern Siqueiros transform deformation zone and have formed as the transform migrated south over the last 1–2 Myr (Gregg et al., 2009; Pockalny et al., 1997).

The tectonic evolution of the region surrounding the Siqueiros fracture zone is characterized by a series of counterclockwise rotations in spreading direction that occurred over the past ~3.5 Myr (Pockalny et al., 1997). These block rotations caused the transform fault to experience local transtensional stresses and undergo extension that may be responsible for the segmentation of the intratransform spreading center, upward melt transport, and the emplacement of the seamount chain along the western trace of the Siqueiros fracture zone (Fornari et al., 1989; Fox & Gallo, 1984; Gregg et al., 2009; Romano et al., 2017). However, the magmatic history and source composition of the volcanic highs, with depths <2,500 m and spaced up to 20–25 km generally running parallel to the Siqueiros fracture zone, is not completely understood. The seamount chain consists of nine main volcanic edifices with varying geometries (Figures 1 and 2). The western portion of the chain (west of 105°W; trending

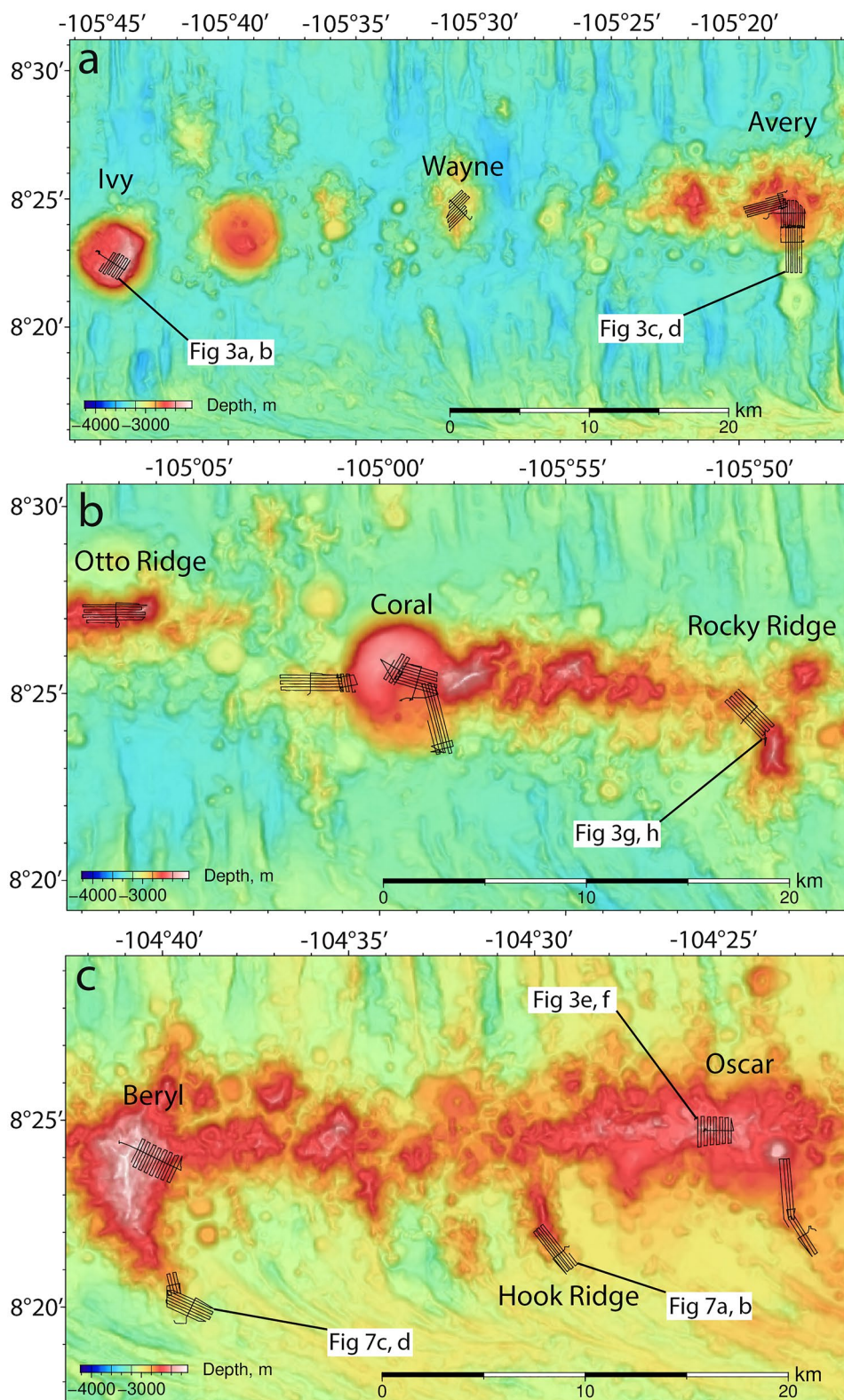


Figure 2. Shipboard multibeam bathymetric data over selected portions of the 8°20'N seamount chain, locations shown in Figure 1; black lines are *Sentry* dive survey tracklines. (a) Distal (western) end with respect to the East Pacific Rise axis including Ivy, Wayne, and Avery seamounts. (b) Central portion including Otto Ridge, Coral seamount, and Rocky Ridge. (c) Ridge-proximal (eastern) end with Beryl, Hook Ridge, and Oscar seamounts.

~264°) from Otto Ridge to Ivy seamount (~96–170 km from the axis), includes larger, more discrete structures with rounded and well-defined craters (up to ~8.6 km in diameter; see Figures 2a and 2b). Here, the individual morphology of the volcanic edifices suggests an age-controlled influence on the volcanism and melting. Between the EPR and ~105°W, the seamounts consist of continuous ridge-like, ~274° trending constructs several kilometers in length, with partially coalesced craters, and small cones (ranging in diameter from ~1.4 to 5.6 km; Figures 2b and 2c). The easternmost seamount in the chain, named Oscar, is located ~22 km from the EPR axis. This proximal portion of the chain (with respect to the EPR axis) is likely to have a more complex history of magmatism, due to overlapping phases of volcanism along the coalesced ridge.

Using major and trace element abundances and radiogenic isotope ratios from *in-situ* rocks sampled using *Alvin* along the 8°20'N seamounts, Anderson et al. (2021) determined that the subridge mantle west of the EPR axis is highly heterogeneous and must melt to variable extents to have created the range of rock types erupted. The composition of mid-ocean ridge basalts (MORB) erupted on-axis is typically relatively depleted in highly incompatible trace element concentrations compared with off-axis seamount lavas, which present a wide compositional range of major element, trace element, and radiogenic isotope ratios (Allan et al., 1987; Batiza & Niu, 1992; Brandl et al., 2012). Lavas from the 8°20'N off-axis seamounts show an extreme degree of chemical heterogeneity, spanning three MORB-type lavas (i.e., normal, depleted, and enriched) that are unrelated to their location along the chain. In addition, they must also have been formed from variable extents of melting of depleted to highly enriched mantle sources (Anderson et al., 2021). These findings suggest that the overall formation of the different portions of the chain was not simply time-transgressive and that most of the seamounts were not generated exclusively by partial melting of a depleted MORB mantle source, which is characteristic in the near-axis region. Therefore, it is important to constrain the relative ages of heterogeneous lavas in order to decipher mantle systematics responsible for forming the off-axis seamount chain.

2. Data and Methods

We report here data collected during RV *Atlantis* cruises AT37-05 and AT42-21 in 2016 and 2018, respectively, over the 8°20'N seamount chain, using AUV *Sentry* for near-bottom sidescan, multibeam, and CHIRP sonar mapping; HOV *Alvin* for observations and sampling, and shipboard sonars for regional mapping. Shipboard multibeam bathymetric data were collected over the entire study area in 2016 using a hull-mounted Kongsberg EM122 sonar, processed using MB-System software (Caress & Chayes, 1996) and gridded at 75 m resolution (Figure 1).

2.1. Near-Bottom Data Collection With AUV *Sentry*

To assess the relative age of volcanic edifices along the 8°20'N seamounts, we use the thickness of sediment draped over the basaltic crust as a proxy for exposure age. Sediment cover here is expected to be minimal because the seafloor is relatively young (0–3 Myr), and average sedimentation rates are expected to be low (i.e., 20–56 m/Myr; Lyle et al., 2002; Rosendahl et al., 1980), since the seamounts are located far from terrigenous sources of sediment. In addition, water depths are ~3,000 m, meaning that the expected meter-scale variations in sediment thickness cannot be resolved using surface vessel-mounted subbottom sonars. We overcome these problems using a variable frequency sub-bottom sonar system mounted on AUV *Sentry*, which provides a stable, noise-free, and well-navigated near-bottom platform to conduct this type of high-resolution acoustic imaging of sediment accumulations.

We analyzed CHIRP, multibeam bathymetric, and sidescan sonar data collected in 2016 from twelve *Sentry* dives on nine seamounts (Ivy, Wayne, Avery, Hook Ridge, Rocky Ridge, Otto Ridge, Coral, Beryl, and Oscar), plus four dives in 2018 that surveyed Coral and Oscar seamounts. We also analyzed seafloor video, still photographic images, and sedimentary push cores collected during HOV *Alvin* diving.

Sentry surveyed at 60–65 m above the seafloor and at a speed of ~0.8–1.0 m/s, acquiring multibeam bathymetric, sidescan sonar, and CHIRP data simultaneously. Navigation was achieved with a Doppler velocity log and inertial navigation system, aided by an ultra-short baseline (USBL) acoustic system, which provided acoustic communication and GPS relative navigation from the surface vessel. Multibeam bathymetric data were acquired during each dive using a 400 kHz Teledyne RESON SeaBat 7125 echo sounder. Figure 3 shows the resulting bathymetric

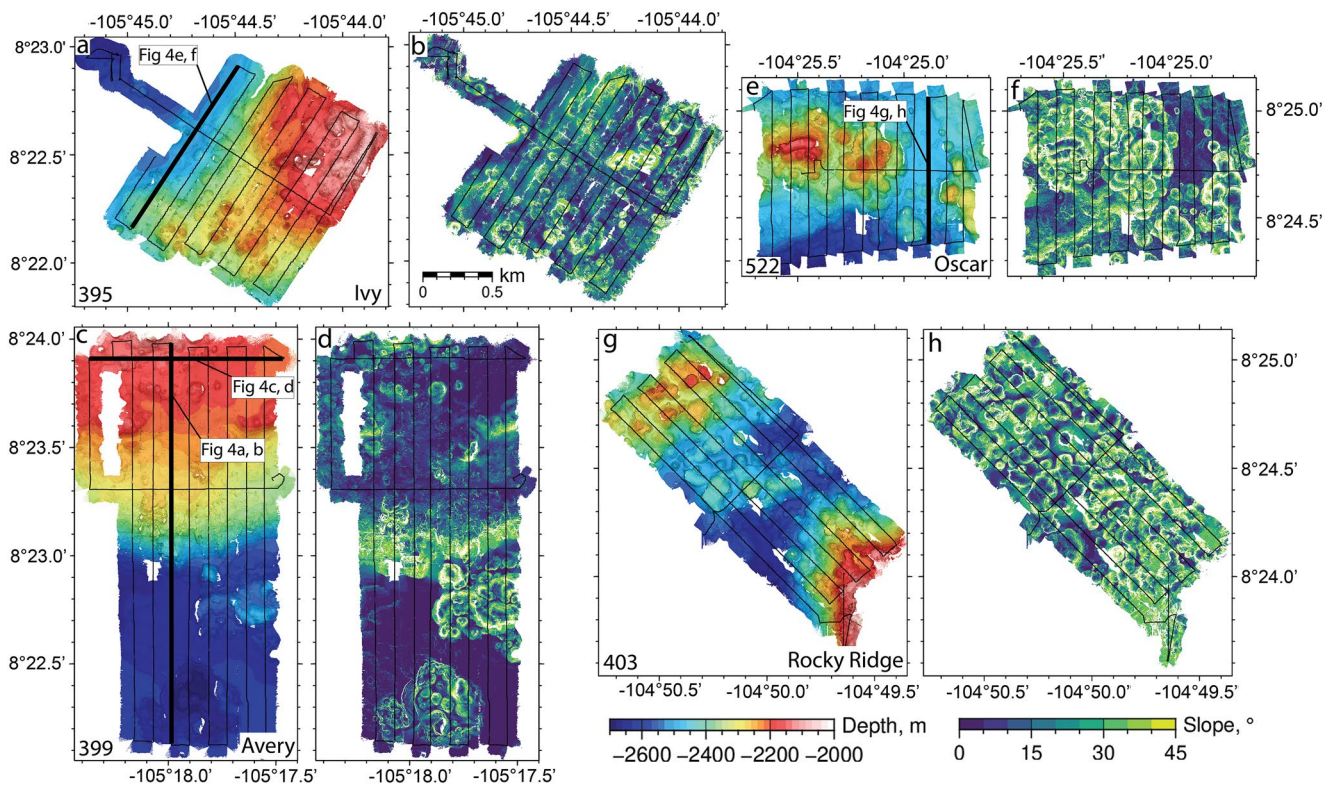


Figure 3. Near-bottom bathymetry and bathymetric slope acquired by *Sentry*; dive numbers noted in the lower left. Thin black lines are survey tracklines; bold lines are examples of CHIRP profiles shown in Figure 4 as noted. (a) and (b) Ivy seamount; (c) and (d) Avery seamount; (e) and (f) Oscar seamount; and (g) and (h) Rocky Ridge. Locations are shown in Figures 1 and 2.

and derived slope data for Ivy, Oscar, Avery seamounts, and Rocky Ridge (*Sentry* dives 395, 399, 522, and 403, respectively). CHIRP data were acquired using an Edgetech 2200M unit operating with a frequency sweep of 4–24 kHz, yielding a vertical resolution of ~ 4 cm. We processed the envelope function of the recorded signal using the Seismic Unix (Cohen & Stockwell, 2013) and MB-System (Caress & Chayes, 1996) software packages. The processing steps included the application of a 0.08, 0.1, 24, and 25 kHz Butterworth filter, automatic gain control and trace balance, with depth conversion (relative to vehicle) using a constant velocity of 1,500 m/s (water). The resulting SEG-Y format data were plotted and interpreted using OpendTect software (dGB Earth Sciences BV; Figure 4). Sidescan sonar data were also collected using the Edgetech 2200M unit operating at a frequency of 120 kHz (Figure 5), in order to further characterize the seafloor.

2.2. CHIRP Data Interpretation

Our objective is to determine the presence or absence of sediment and where present, its thickness. Where sediment is present, the seafloor reflection is spatially continuous and bright in amplitude, due to the acoustically smooth seabed causing minimal scattering of energy at the water-sediment interface (Figure 4). Where sediment is absent, the seafloor reflection is lower in amplitude and more chaotic, due to the scattering effects of uneven volcanic terrain such as pillowed and lobate lava flows and volcanic rubble and talus. This contrast in seafloor reflectivity allows us to determine whether sediment is present or absent. Beneath the high amplitude seafloor reflection, sedimentary layers are often acoustically transparent, beneath which the basement reflection is often diffuse, weak, and noisy in character. No coherent reflectivity is seen below the sediment-basement interface, due to rapid attenuation of acoustic energy in volcanic layer 2A (Christeson et al., 2019). Where seafloor and basement reflections can be identified, we can estimate the sediment thickness along all tracklines for each *Sentry* dive. To account for the two-dimensional nature of the CHIRP profiles, we interpolate between survey lines, using a nearest neighbor algorithm to assign an average thickness value to nodes that have one or more points within 50 m centered on the node. This interval was chosen as a compromise between trackline spacing and

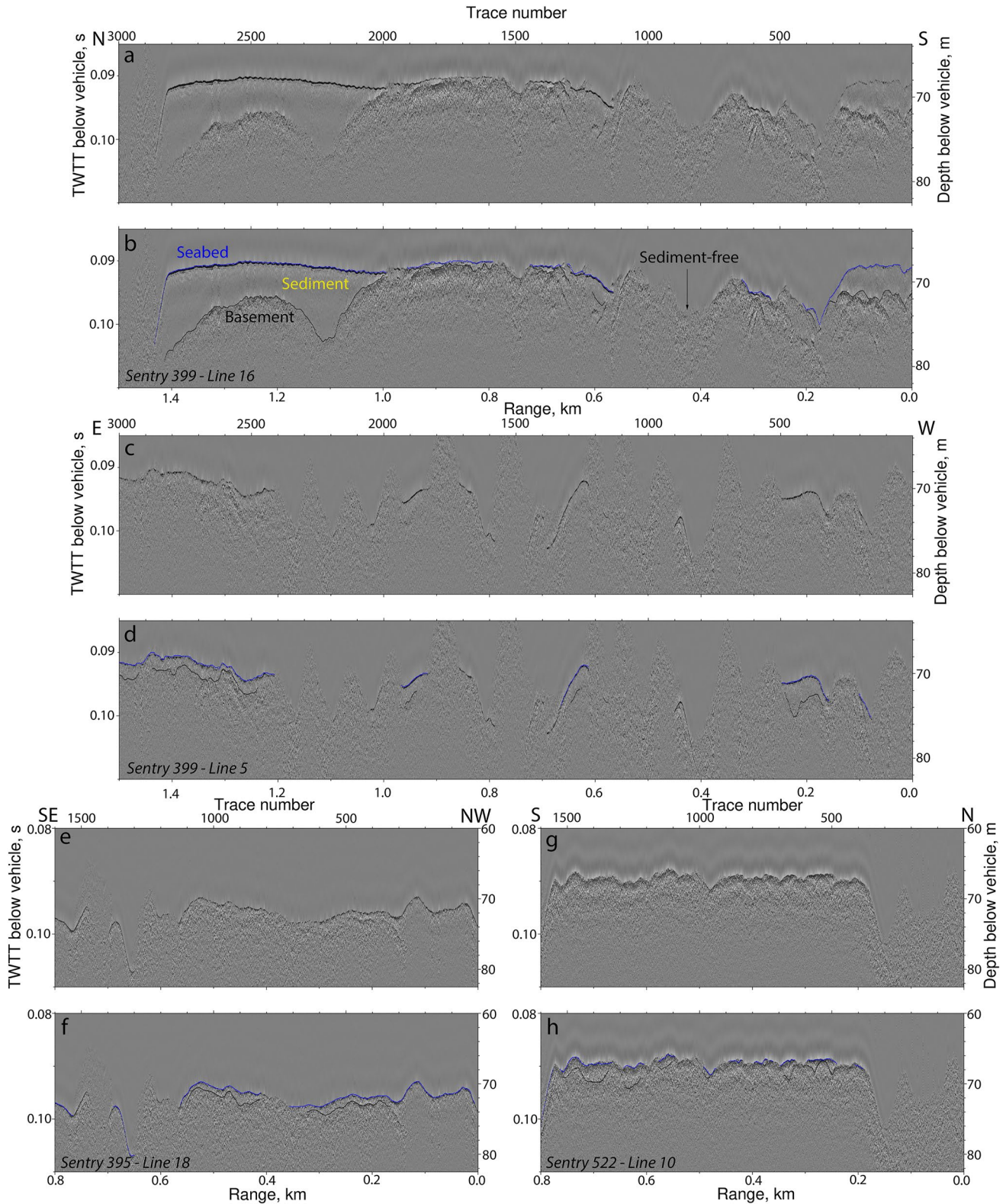


Figure 4. Examples of CHIRP profiles acquired by *Sentry* along the 8°20'N seamounts, locations shown in Figure 3. (a, c, e, and g) Uninterpreted profiles; note vertical axis plotted relative to vehicle position, as two-way travel time (left y axis) and converted to depth (right y axis), assuming velocity of 1,500 m/s (b, d, f, and h) Interpreted versions. Blue lines mark high amplitude seabed reflection overlying acoustically transparent sediment; black lines are top of volcanic basement. In (b), note ~2–10 m thick sediment pond above volcanic basement between traces 2,000–2,800, and an apparently sediment-free seafloor between traces 700 and 1100. In (f), note the lack of basement reflection, which implies sediment of indeterminate thickness between traces 0 and 300.

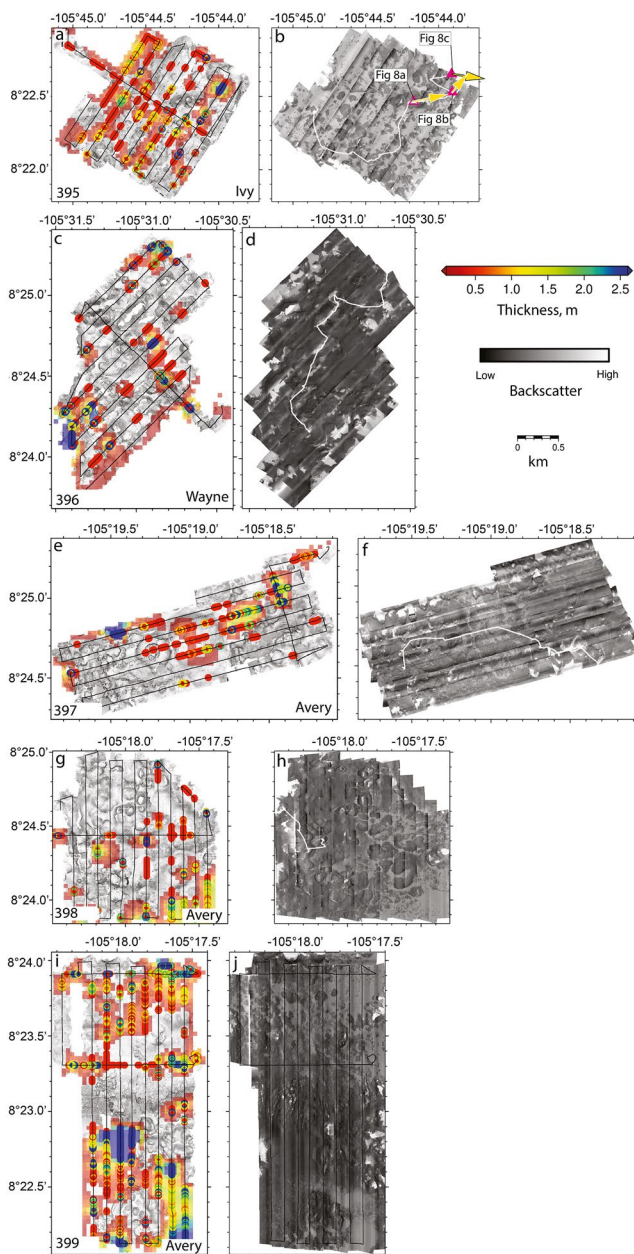


Figure 5. (continued). Bathymetric slope overlain with sediment thickness estimates from CHIRP profiles and side-scan sonar images acquired by *Sentry*, with dive numbers (lower left) and seamount names (lower right) noted. Thin black lines are survey tracklines; open circles colored according to point estimates of sediment thickness; shaded colors show interpolated thickness grid calculated using adjustable tension continuous curvature splines with 50 m node spacing, and a tension factor of 0.35. Note that thickened sediment is mainly observed in bathymetric depressions or areas of low relief. (a) and (b) Ivy seamount. (c) and (d) Wayne seamount. (e, f, g, h, i, and j) Avery seamount (k) and (l) Otto Ridge (m, n, o, p, q, and r) Coral seamount (s) and (t) Rocky Ridge (u, v, w, and x) Beryl seamount (y) and (z) Hook Ridge (aa, bb, and cc) Oscar seamount. White lines indicate HOV *Alvin* navigation tracklines; open/filled purple triangles are location of photographic images/push cores, respectively, taken by *Alvin*, and shown in Figure 8; yellow arrows indicate *Alvin* heading.

spatial continuity, and is broadly consistent with the tens of meter characteristic wavelength of local bathymetric highs and lows across the survey areas.

3. Results

We use a combination of regional multibeam bathymetric data, sediment thickness from CHIRP profiles, and seafloor character from near-bottom multibeam data, sidescan sonar images, and near-bottom imagery collected using *Alvin* to characterize volcanic morphology and sediment distribution along the seamount chain.

3.1. Regional Seafloor Fabric

The dominant seafloor fabric on either side of the EPR axis between Clipperton and Siqueiros FZs comprises abyssal hill structures that are primarily aligned along the $\sim 350^\circ$ trend of the EPR axis (Edwards et al., 1991; Goff, 1991). The exceptions to this pattern are curved structures and pseudo-faults that demark the trajectory of the $9^\circ 03' N$ overlapping spreading center (Carbotte & Macdonald, 1992; Carbotte et al., 2013; Klein et al., 2013; Wanless & Shaw, 2012; White et al., 2009).

North of the $8^\circ 20'$ seamount chain, abyssal hills are subparallel and generally north-south trending, while south of the chain they curve from EPR-parallel adjacent to the seamounts to east-trending toward the ridge-transform intersection, merging into the Siqueiros FZ. These differences in orientation suggest continued magmatic activity during plate motion to the west (see Figures 1 and 2c). South of the zone of curved seafloor fabric, there are areas where seafloor resembles subsets of intratransform spreading center terrains. This terrain could have formed within the transform zone and has been later deformed and moved westward where it now represents the northern margin of the Siqueiros FZ. These observations are consistent with previous suggestions that during tectonic reorganization of the fracture zone over the past 1–2 Myr, volcanism has persisted in the area south of the $8^\circ 20' N$ seamounts (Pockalny et al., 1997).

The $8^\circ 20' N$ seamount chain is composed of a diverse array of volcanic constructs ~ 200 – 900 m in height above the surrounding seafloor. Several east-west trending, nearly continuous ridges of coalesced volcanoes can be identified, along with numerous smaller cones and mounds on the summits and basal aprons of the seamounts. Also evident are EPR-parallel constructs that appear to have a central volcano with rift zone ridges that primarily extend south from the seamount summit, and larger, individual volcanoes that have craters and calderas (Figure 1). In some cases, volcanoes in the chain have coalesced along east-west lineaments to form constructional ridges, suggesting that the timing of magmatism and volcanism has been episodic in terms of erupted volume relative to spreading rate. There is good morphological and observational evidence for recent volcanism even on some of the edifices near the middle of the chain, nearly ~ 100 km from the EPR axis (Anderson et al., 2021). Rift zone-like extensions of constructional volcanism that trend south-southeast from the main edifices in the eastern half of the chain suggest sustained magmatic supply (over hundreds of ka), during which the central volcanoes grew, while some developed their elongated (north-south) shapes. These fabrics indicate that volcanism was influenced by spreading dynamics, as the seafloor was deformed along the northern margin of the Siqueiros FZ and south of the seamount chain.

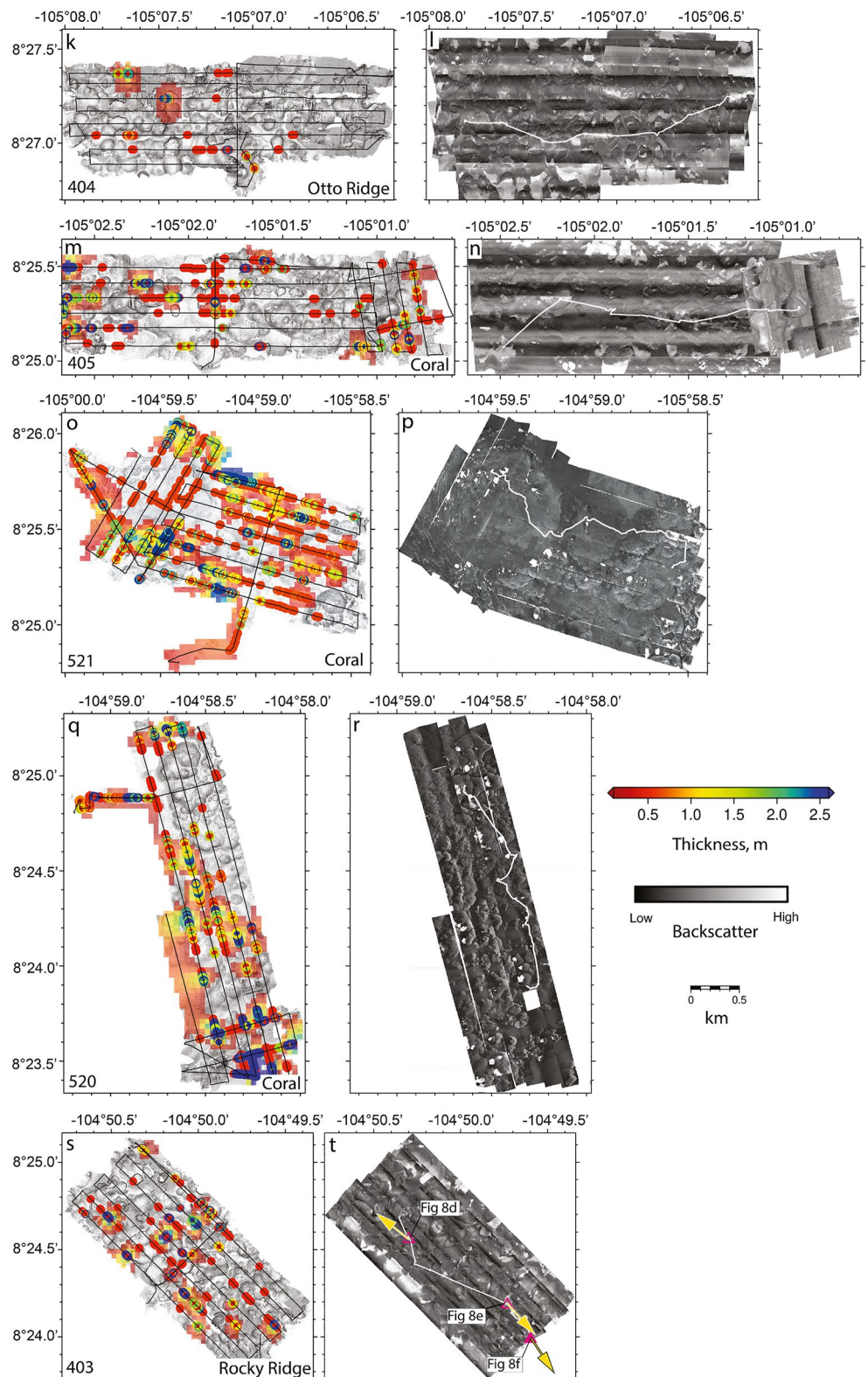


Figure 5. (Continued)

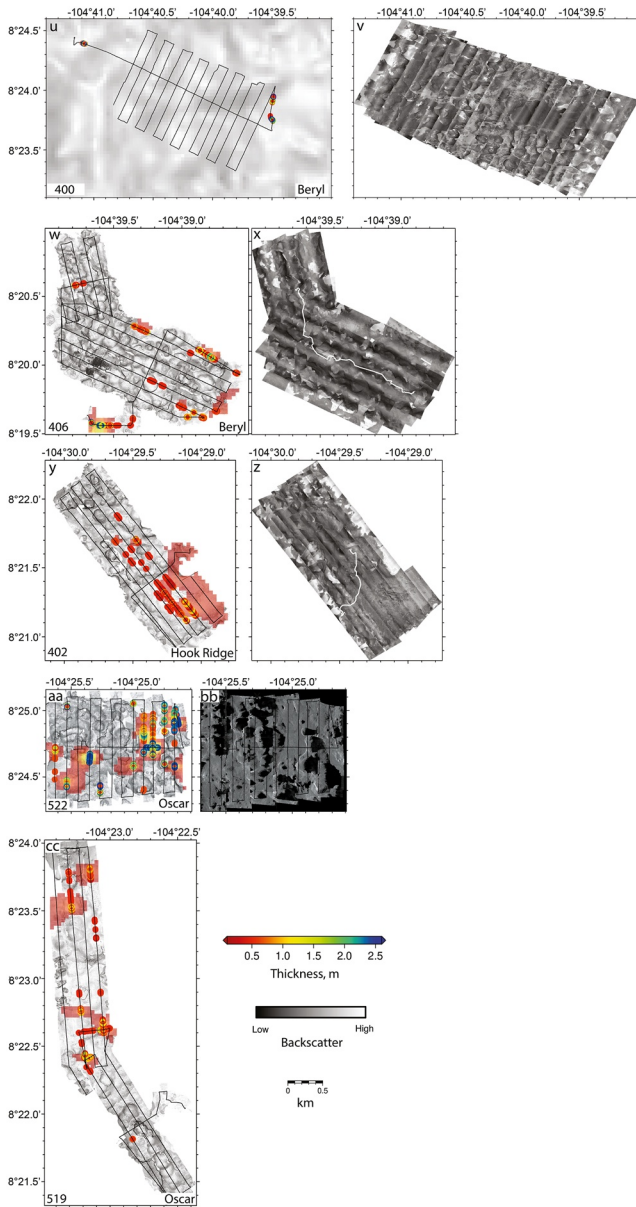


Figure 5. (Continued)

3.2. Local Sediment Thickness Variations

Sediment is distributed unevenly at each individual volcanic edifice and varies in thickness between edifices. Sediment is typically ponded in bathymetric lows, and in low relief areas (Figure 5). From west to east, the portion of the chain distal to the EPR hosts three prominent volcanic structures: Ivy, Wayne, and Avery seamounts (Figures 2a and 5). Ivy is the most distal seamount, located ~ 170 km from the EPR axis on oceanic crust nominally ~ 3 Myr in age. Ivy consists of an individual, symmetric, and cone-shaped edifice with a basal radius of ~ 3.2 km and ~ 990 m of relief above the surrounding seafloor. The local summit morphology shows an eastern high composed of smaller, circular-shaped mounds (each ~ 150 m in diameter), separated by interconnected low relief corridors, gently dipping westward. Sediment cover is mainly restricted to the summit (Figure S1 in Supporting Information S1), where it is up to ~ 2 m thick, lying mainly on the western, deeper edge of the seamount (*Sentry* dive 395; Figures 3a and 3b and Figures 5a and 5b). However, some deposits thicker than 3 m are observed in the shallower eastern section (Figures 5a and 5b).

Wayne seamount is also an isolated volcanic structure, with a north-south elongated, lenticular shape ~ 8.3 km long, ~ 4.9 km wide, and with ~ 620 m of maximum relief. Wayne's summit includes a northward-dipping high, with several sparsely spaced cones to the north. We observe a similar depositional pattern to Ivy at Wayne seamount (*Sentry* dive 396; Figures 5c and 5d), located ~ 140 km from the EPR axis on ~ 2.6 Myr-old crust, where up to ~ 5 m of sediment is deposited on the south-western flank. The central and northern summits at Wayne seamount have sparse sediment accumulations, typically ~ 1 m thick.

Avery seamount, located ~ 120 km from the EPR on ~ 2.2 Myr-old crust, has an irregular morphology (roughly 11.2×10.4 km in size, with ~ 845 m of maximum relief). Avery is the westernmost partially coalesced seamount in the chain, with volcanic constructs that continue southward and connect with north-south trending abyssal hills toward the Siqueiros FZ. Sediments are concentrated on the shallow summit of the upper western flank (*Sentry* dive 397; Figures 5e and 5f), where the slope is gentler, and includes small local depressions. Avery's summit is characterized by several circular volcanic mounds with ~ 50 m relief and 150–200 m in diameter, surrounded by low relief areas, where sediments are 1.5–3 m thick (*Sentry* dive 398; Figures 5g and 5h). The southern flank of Avery seamount is covered with sediment up to 9–10 m thick (*Sentry* dive 399; below ~ 0.09 TWTT, see Figures 4a and 4b, and Figures 5i and 5j), but is thin or absent around the circular volcanic constructs to the north.

The central portion of the seamount chain hosts Otto, Coral, and Rocky Ridge, which consist of cones and partially coalesced craters (Figures 2b and 5). Otto Ridge (*Sentry* dive 404; Figures 5k and 5l) is situated on ~ 1.8 Myr-old oceanic crust, ~ 95 km from the EPR axis. Otto Ridge extends over ~ 20 km from west to east and ~ 7.6 km from north to south, with ~ 630 m of relief. Notably, Otto coincides with a change in the overall orientation of the $8^{\circ}20'N$ seamount chain at around $105^{\circ}W$, where the seamounts change from trending $\sim 264^{\circ}$ west of Otto, to 274° east of that seamount (see Figure 1). Sediment is mostly concentrated at the base of the flat-topped ridge at Otto, with relatively little sediment on the flanks (Figure S1 in Supporting Information S1).

Coral seamount (*Sentry* dive 405, 520, and 521; Figures 5m and 5n) is located ~ 80 km from the EPR, with a nominal crustal age of 1.5–1.6 Myr. Coral is a near-symmetric circular volcanic cone that has an apparent volcanic breach toward the southeast, ~ 3.3 km in radius and with ~ 865 m of relief. However, Coral appears to be connected to a hummocky ridge of coalesced highs that continues eastward toward the EPR. Coral's summit,

topped with a circular volcanic cone, and upper southern slopes, are covered in near continuous sediment, while the lower flanks have sparse local sediment ponds up to ~10 m thick, and the western flank up to 3 m thick.

Rocky Ridge (*Sentry* dive 403; Figures 3g and 3h and Figures 5s and 5t) is ~67 km from the EPR axis on ~1.2 Myr-old crust and has a maximum relief of ~466 m from the seafloor. Rocky Ridge is located ~17.5 km from the eastern edge of the hummocky ridge that connects with Coral. The summit consists of a relatively low relief plateau, overlain by sediment with little evidence of ripples on the seabed (see Figure 5f). Although the majority of the sediment there is concentrated in the local central basin with thicknesses up to ~3 m, local bathymetric highs are also partially sediment-covered, with accumulations in low relief areas between individual volcanic mounds (see Figures 5d and 5e and Figure S1 in Supporting Information S1).

The portion of the 8°20'N seamount chain proximal to the EPR axis consists of Beryl, Hook Ridge, and Oscar seamounts. The easternmost region of the chain consists of complex and localized overlapping structures that form continuous, coalesced, and elongated volcanic constructs. The southern flanks of constructs in the easternmost part of the chain generally have higher relief than northern flanks, and southern flanks often have arcuate morphologies bending eastward toward the EPR axis (such as other subparallel seafloor topographic features, see Figures 1 and 2c), which suggests increasing tectono-magmatic influence from the interaction with motion of the Siqueiros transform fault. Beryl seamount is located approximately 50 km from the EPR axis on 0.9–0.8 Myr-old crust (*Sentry* dives 400 and 406; Figures 5u–5x), and it is the larger edifice, extending ~15.5 km north-south with a maximum elevation of ~1,070 m from the surrounding seafloor. Beryl's southern flank has an articulated morphology extending south ~9.2 km from the summit and the main seamount trend. The northern flank appears steeper than the southern flank, which extends further downslope into a local basin. Beryl's summit hosts some scattered sediment pockets <1 m in thickness, which thicken in local depocenters on the southern flank (Figure 5). Hook Ridge is oriented roughly north-south at ~30 km from the EPR, on crust ~0.5 Myr in age, and is ~5 km south of the main seamount trend (*Sentry* dive 402; Figures 5y and 5z). Most of the sediments on Hook Ridge are on a southeast trending slope (Figure S1 in Supporting Information S1), although their maximum thickness does not exceed 1 m. Oscar seamount, the closest volcano to the EPR axis (~20 km) is at the eastern termination of the chain on 0.4–0.3 Myr-old crust. Oscar has an overall circular morphology, like that of Coral, with a ~3.5 km radius and ~590 m of maximum relief. Oscar's flat-topped summit hosts two low relief volcanic highs (Figures 3e and 3f), where sediment is mostly absent (Figures 5a and 5b). On the eastern side of Oscar seamount, sediment is up to ~3 m thick and fairly evenly distributed in low relief basins. Oscar's southern flank, where most of the sediment has accumulated, has a gentle slope with sparse circular volcanic mounds surrounded by relatively thin (<1 m) sediments (Figure 5c and Figure S1 in Supporting Information S1).

3.3. Gravitational Mass Wasting

After primary deposition, sediments are likely to be reworked by the combined effects of mass wasting and deep-water current activity. Gravitational mass wasting is expected on slopes with an angle of repose steeper than ~20–30° (Cannat et al., 2013), examples of which can be found on the flanks of the 8°20'N seamounts. Destabilized sediment is most likely to accumulate in low relief areas and local basins near the base of bathymetric highs. Since the degree of mass-wasting is likely to be controlled by slope and relief, in Figure 6 we compare sediment thickness estimates to three metrics that reflect the slope environment: (a) bathymetric slope, calculated as magnitude of the vector gradient of the 1-m resolution near-bottom multibeam bathymetric data; (b) relative relief, defined as the depth difference (i.e., vertical distance) between a point in question and the deepest point on the seamount, normalized with respect to the total relief of the seamount; and (c) depositional setting, classified by an analyst (and somewhat subjectively) as summit, flank or local basin, identified after local morphological analysis of subenvironments for each volcanic edifice.

Avery, Coral, and Beryl seamounts provide useful examples of this approach, with sediment thickness estimates on a range of slope gradients and representing all three depositional settings. Avery is a flat-topped seamount with a circular conic shape and gentle flanks where the sediment mainly accumulates on low-gradient settings located both at the summit and the intermediate slope (Figures 6a and 6b). A larger fraction of sediment volume is observed at the seamount summit (Figure 6c). Similarly, Coral has a flat plateau topping a circular morphological edifice with steep flanks, and even though it is part of a series of coalesced seamounts, sediment is concentrated in high relief areas and on the summit (Figures 6d–6f). In contrast, Beryl has an irregular morphology and a

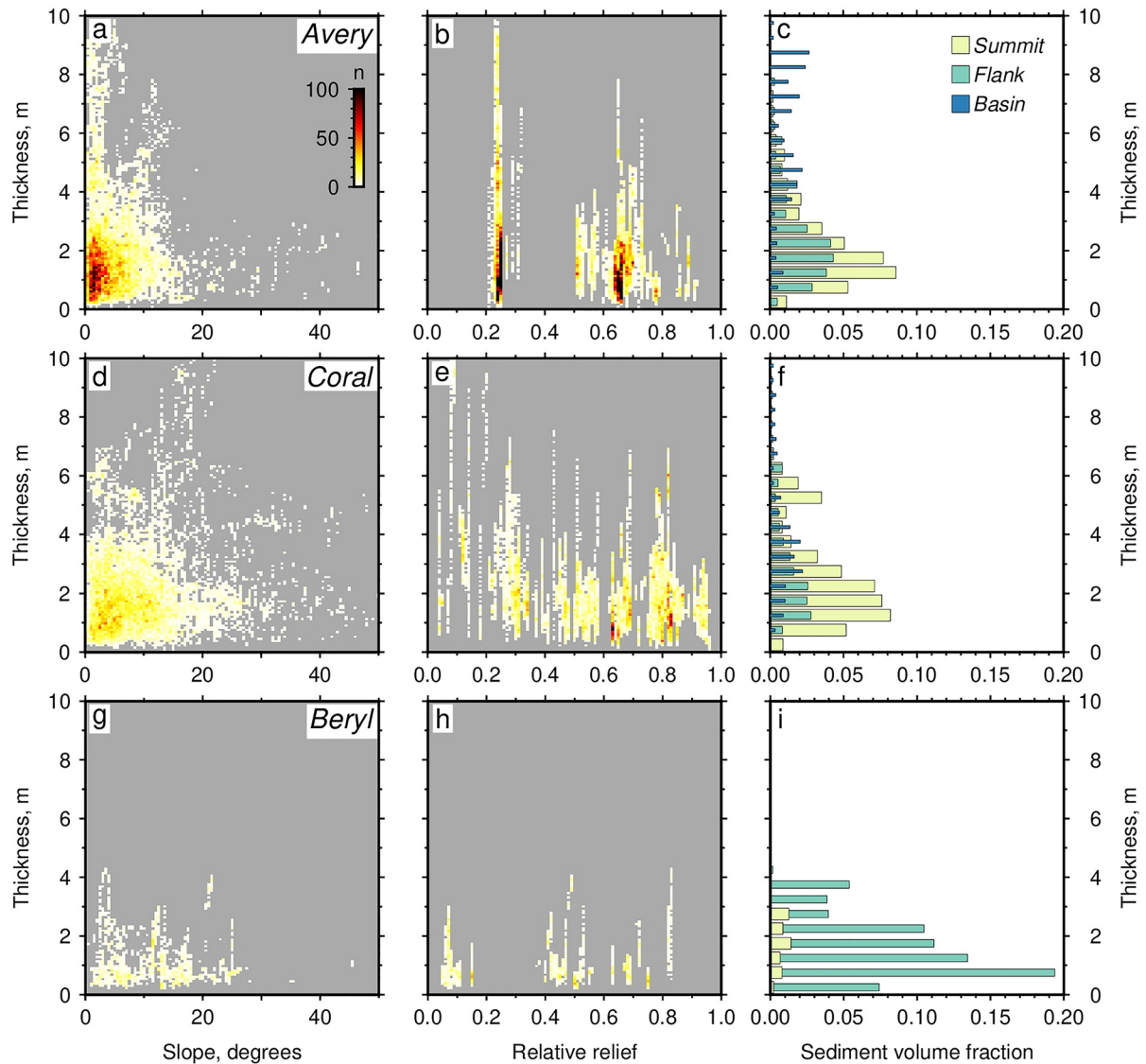


Figure 6. Sediment thickness distribution versus three parameters relating to potential for currents and mass-wasting, for Avery, Coral, and Beryl seamounts. (a, d, and g) bathymetric slope; (b, e and h) relative relief, defined as the normalized relief, with respect to seamount summit, where 0 = at base and 1 = at summit; (c, f, and i) volume fraction of sediment grouped by depositional setting (i.e., summit, flank, or local basin).

relatively flat summit, a steep northern slope, and a gentler southern flank. Here, most of the sediment fraction is located on the southern flank, with only small volumes at the summit (Figures 6g–6i).

3.4. Bottom Current Activity

The interior of the Pacific Ocean is located far from terrestrial sources of sediment, and strong directed motions of seawater such as the Humboldt and South Equatorial currents are unlikely to exert significant influence (Lyle et al., 2002). Nonetheless, strong bottom currents may focus into the bathymetric lows between seamounts, causing erosion and redeposition of sediments. Tidal activity can affect sediment redistribution, especially through the interaction with seamount morphology, although the extent of current activity and sediment re-suspension here is not known (Turnewitsch et al., 2013). The Circumpolar Deep Water gyre flows eastward around 15°N where it turns southwest on the west flank of the EPR toward the equator (Johnson & Toole, 1993; Mantyla, 1975; Tsuchiya & Talley, 1998). Additionally, studies of ocean currents at 9–10°N segment on the EPR show clockwise circulation, with northward flow along the western flank and a southward flow along the eastern flank

(Xu et al., 2018). Turbulence of oceanic overturning circulation is expected to be directly proportional with seafloor topographic roughness (Kunze et al., 2006; Polzin et al., 1997). Therefore, while uneven bathymetry at slow-spreading centers is expected to result in a high degree of turbulence, faster-spreading ridges such as the EPR, being bathymetrically smoother, are expected to be associated with lower turbulence. Observations from the Lamont seamount chain near 10°N west on the EPR show that horizontal current velocities in the narrow deep passages between seamounts and near the peaks can be high, up to 10–20 cm s⁻¹ (Thurnherr et al., 2011). Turbulence levels are also elevated by up to an order of magnitude above background in these areas, suggesting that sediment winnowing is likely (Thurnherr & St. Laurent, 2011). Weaker currents may also play a role in the dispersal of suspended sediment prior to settling and accumulation, meaning that erosion and winnowing may not be necessary to remobilize sediment grains near the seafloor. Slow, steady, and frictionless fluid flow above an isolated bottom obstacle, such as a seamount, can result in stagnant fluid in the entire column of fluid directly above the obstacle, known as a Taylor cap (Lavelle & Mohn, 2010). Therefore, the formation of a Taylor caps on seamount summits may play a role in particle retention, although are not ubiquitous since most ocean settings are not dominated by a single steady flow component.

To our knowledge, there are no direct seafloor current velocity measurements at the 8°20'N seamounts. We investigated ocean circulation above the 8°20'N seamounts using shipboard acoustic Doppler current profiler (ADCP) data collected during cruise AT37-05. Although there are possibly elevated current velocities above Beryl seamount (Figure S3b in Supporting Information S1), we cannot resolve the presence of anticyclonic and cyclonic vortices since ADCP velocity data do not extend below ~600–800 m. Hence, these data provide only a limited insight into current motions and the Taylor cap effect above the seamounts, which are situated at water depths in excess of ~3,000 m (Figures S3 in Supporting Information S1). We also investigated the possibility of current variations on diurnal, decadal, and seasonal timescales, using simulations from the data-assimilative hybrid isopycnal-sigma-pressure coordinate ocean model (HYCOM; Bleck et al., 1992; Halliwell et al., 1998, 2000). HYCOM model hindcast data extracted at a sequence of time intervals at 3,000 m depth and at the seabed do not indicate consistent diurnal, decadal, or seasonal variability (see Figures S4–S8 in Supporting Information S1), with current speeds below 0.15 m/s, indicating that sediment redistribution is unlikely. Our hindcast results show that while current speeds do vary across the seamount chain at different times of the year, these patterns vary both in space and time, with no area favored for elevated current speeds over another. These hindcast results cannot definitively confirm or rule out the effects of current activity, for two reasons. First, the bathymetric grid used as input to HYCOM models does not resolve either the Siqueiros fracture zone nor the 8°20'N seamount chain (Figure S9 in Supporting Information S1), and hence, detailed interpretation of current speed variations associated with the seamount chain or the fracture zone is not feasible. Second, there is doubt about the degree to which modern current speed and pathways are relevant, since the sediment thickness data contains an integrated record of deposition, erosion, and tectonic evolution over 3.2 million years. Hence comparison with modern ocean circulation model hindcasts, which represent regional-resolution snapshots representing modern timescales of months or decades, remains speculative.

In order to qualitatively assess local water motions, we use the azimuthal deviation between *Sentry* vehicle heading and navigation-derived tracklines (i.e., crabbing angle) as a proxy for current strength (Figure 7). Although trackline orientation bias means that the orientation of the estimated vector field of the flow is uncertain, the difference between the heading and navigation tracklines is a qualitative indicator of current strength, and hence an indicator of the potential for sediment erosion and redistribution at the time of data acquisition. On three dives at Hook Ridge, Beryl, and Coral seamounts (*Sentry* dives 402, 406, and 521, respectively), we find a median heading deviation higher than 4° (Table S1 in Supporting Information S1), likely due to currents influencing vehicle heading (Figures 7b and 7d). For the other 12 dives analyzed, we found negligible heading deviation (Table S1 and Figure S2 in Supporting Information S1). We find that areas with greater heading deviation are mostly sediment-starved, while low deviation zones typically have thicker sediments. For example, at Hook Ridge, we find vehicles heading deviated toward the east, in the northern area of *Sentry* dive 402 (Figure 7a). In contrast, the southern portion of the survey area at Hook Ridge shows lower heading deviation, corresponding to thicker sediment deposits. Similarly, we find relatively higher heading deviation in the western side of Beryl seamount (*Sentry* dive 406; Figure 7c) corresponding to an area devoid of sediment, while lower attitude deviation on the eastern side of the seamount has sparse sediment.

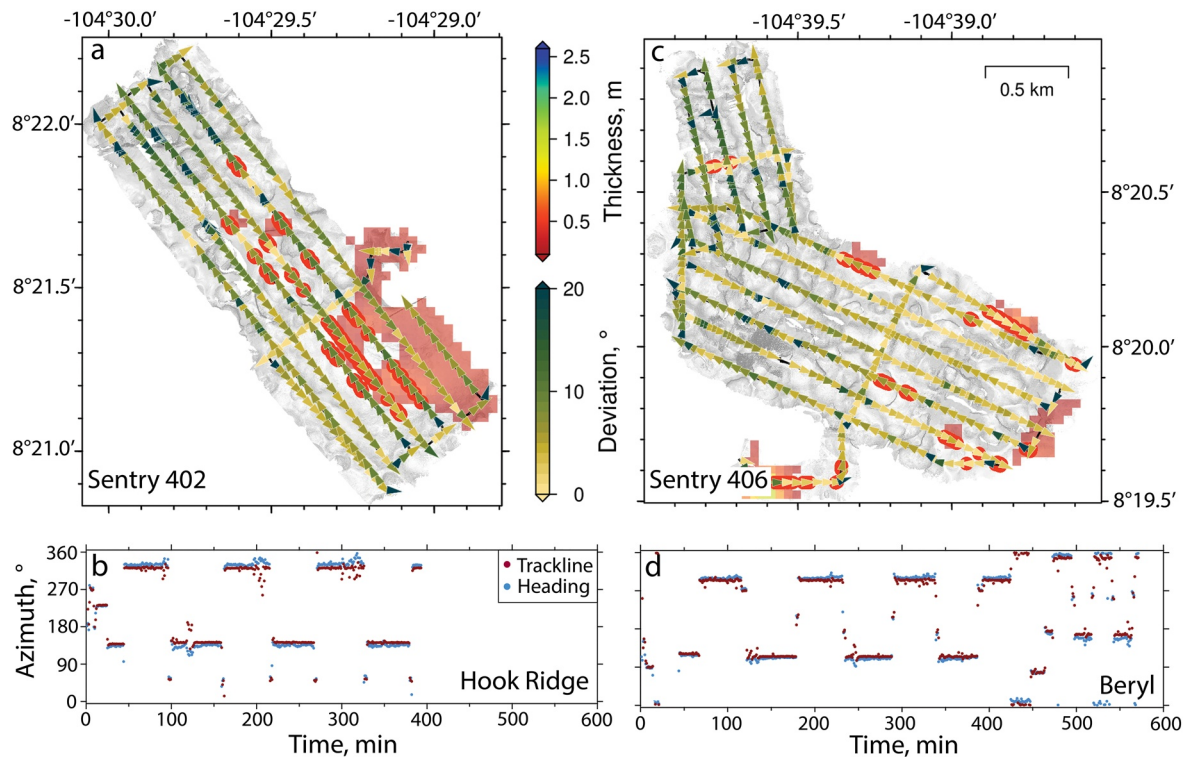


Figure 7. Sentry heading versus navigation tracklines azimuth, which is a tentative proxy for current strength. (a) and (c) Maps showing bathymetry overlain with interpolated sediment thickness grid and navigation tracklines, respectively on Hook Ridge and Beryl seamounts. Arrows are vehicle heading, color indicates deviation between vehicle heading and trackline orientations. (b) and (d) Time series plots of heading versus navigation direction represented by blue and red dots, periods of mismatch suggest influence of strong bottom currents on vehicle dynamics. Locations shown in Figure 2c.

While we acknowledge this current strength proxy is qualitative, the good match between areas of low heading deviation and thicker sediment (and vice versa), implies that, at least at the time of the survey, we do not expect strong current activity at the summits of Ivy, Wayne, Avery, Otto Ridge, Rocky Ridge, and Oscar seamounts.

3.5. HOV *Alvin* Dive Photographic Images

To help ground truth our sediment interpretation from the CHIRP and sidescan sonar data, we use still frame images collected using a DeepSea Power and Light 4K video camera and a Multidisciplinary Instrumentation in Support of Oceanography GoPro 12 MP still camera mounted on HOV *Alvin*. Example seafloor images from Ivy seamount and Rocky Ridge (*Alvin* dives ALV4848 and ALV4856, respectively) are shown in Figure 8. At Ivy seamount, the images show volcanic hummocks composed of pillow lavas and basaltic lavas outcropping between scarce sediment (Figure 8a), which agrees well with the sediment-poor area identified from the CHIRP data in Figure 5b. The seafloor sediment often contains ripples lying on low relief areas and localized sediment accumulations surrounded by volcanic cones at the summit of the edifice (Figures 5b and 8b). Sediment ripples are frequently symmetric and approximately linear, often with well-defined margins and low relief (Figures 8b and 8c). The sediment ripples are likely to be similar to soft-bottom undulations commonly seen elsewhere, generated by oscillatory wave motion that is able to locally transport fine-grained sand (e.g., Lonsdale & Spiess, 1977). Such ripples are diagnostic of a low-energy environment with weak current activity and likely formed in presence of a gentle slope (Harms, 1969). However, Figure 8f shows a flat plateau without evident sedimentary features on Rocky Ridge, suggesting the absence of bottom currents, whereas in Figures 8d and 8e there are basaltic exposures with thin sediment patches.

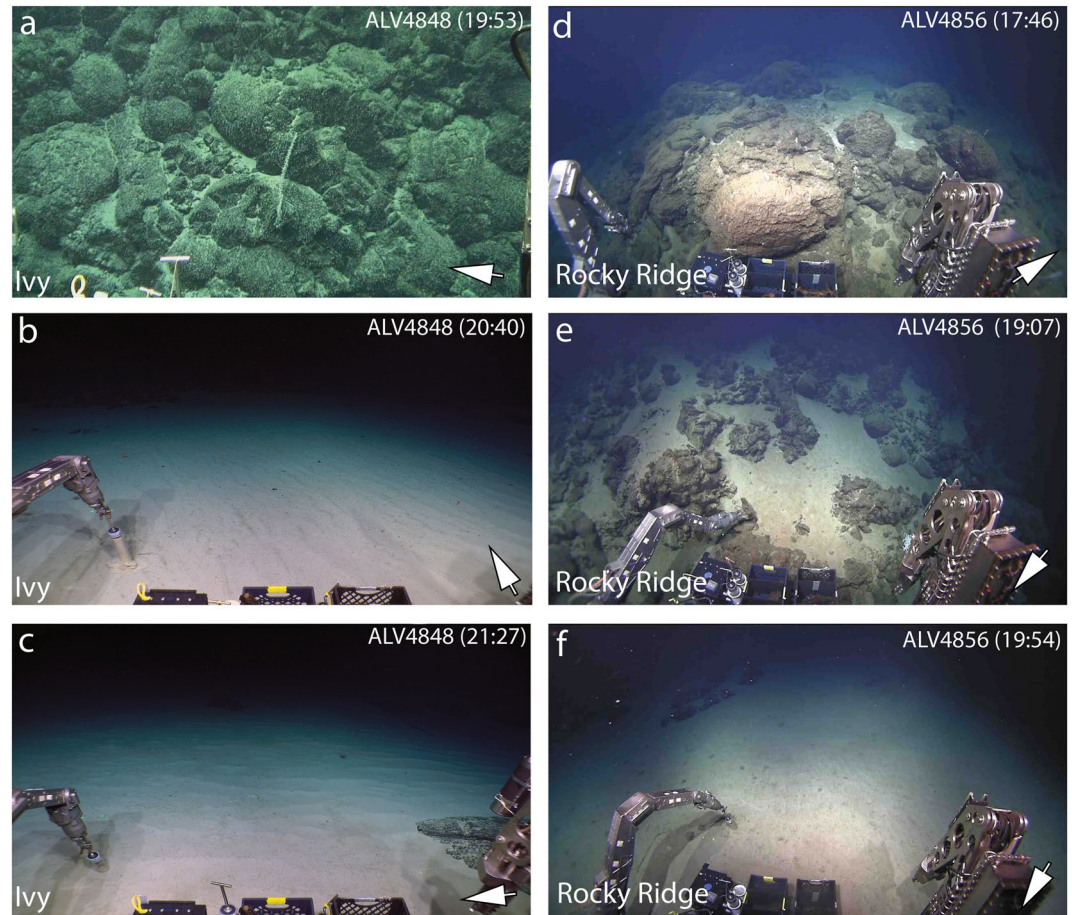


Figure 8. Seafloor photographs taken using cameras mounted on HOV *Alvin* at Ivy seamount and Rocky Ridge, with dive numbers and times noted; white arrow indicates north direction; field of view is ~ 2 m wide in (a) and is ~ 3 m in subsequent panels. (a) Volcanic basement outcrop, Ivy seamount. (b) Push core into fine-grained sand and silt, Ivy seamount. (c) Ripples, ridges of sediment and a basaltic pillow exposed on the right, Ivy seamount. (d) Rounded basaltic mound summit, Rocky Ridge. (e) Isolated sediment accumulation between small local basement ponds, Rocky Ridge. (f) Spatially extensive sediment cover, with little apparent depositional traces, Rocky Ridge. Locations shown in Figure 5.

3.6. Sediment Thickness Variation Across the $8^{\circ}20'N$ Seamount Chain

We calculate the mean sediment thicknesses for each dive (Figure 9) using thickness values from CHIRP profile interpretation where the top and bottom sediment layers have been identified (Figure 4). Bathymetry data and slope maps show that most sediment is located in low-lying or relatively flat areas, while the shallower areas of each seamount are mainly sediment-starved. However, the mean sediment thickness variation does not follow a constant trend along the chain. Figures 9 and 10 show that sediment thickness variations are not proportional to the distance from the ridge axis (i.e., nominal crustal age) and position along the chain. At Ivy, Avery, Rocky, and Oscar seamounts, the sediment is dominantly deposited on the deepest and flat areas.

In order to compare sediment thickness between seamounts, we estimated a normalized mean sediment thickness by summing the sediment total volume across each *Sentry* dive, divided by each total areal coverage, resulting in a spatially averaged sediment thickness estimate. The histograms shown in Figure 9 present the variability of the sediment with the mean, standard deviation, and number of measurements. From the proximal to the distal seamounts along the $8^{\circ}20'N$ chain, mean sediment thickness does not increase progressively with distance from the EPR. Near to the EPR, Oscar's south flank and summit have mean sediment thicknesses of 0.8 and 2.1 m, respectively, Hook Ridge has a mean sediment thickness of 0.6 m, while Beryl's summit and south flank have thicknesses of 0.4 and 1.1 m, respectively (Figures 9k–9o). To the west along the seamount chain, mean sediment thickness at Rocky Ridge is greater, with values up to ~ 2.5 m (Figure 9j) and at Coral (Figures 9g–9i),

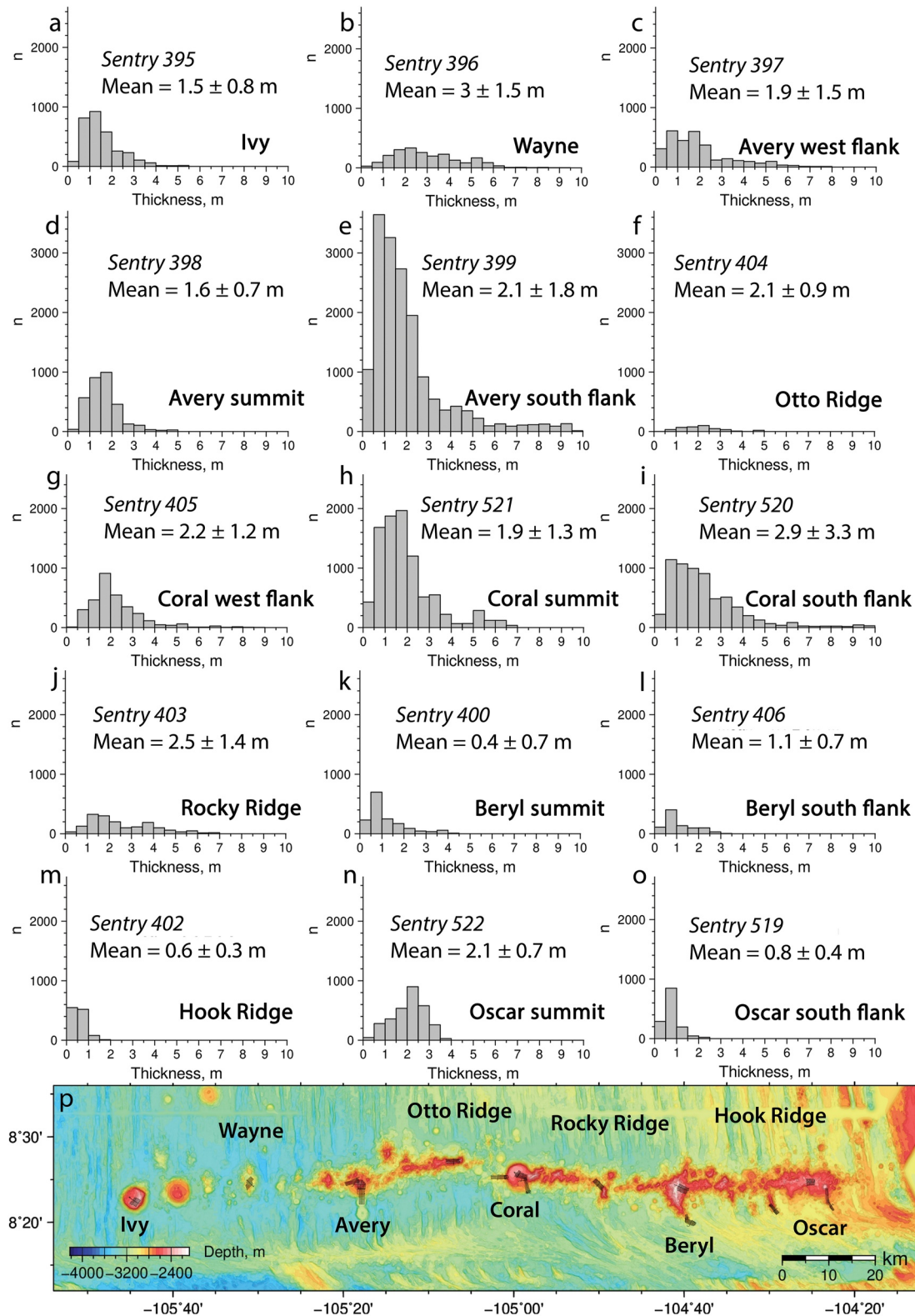


Figure 9. (a–o) Histograms showing sediment thickness along 8°20'N the seamount chain for each *Sentry* dive. Seamount names and *Sentry* dive numbers noted; mean thicknesses noted $\pm 1 \sigma$. (p) Bathymetry with seamounts noted.

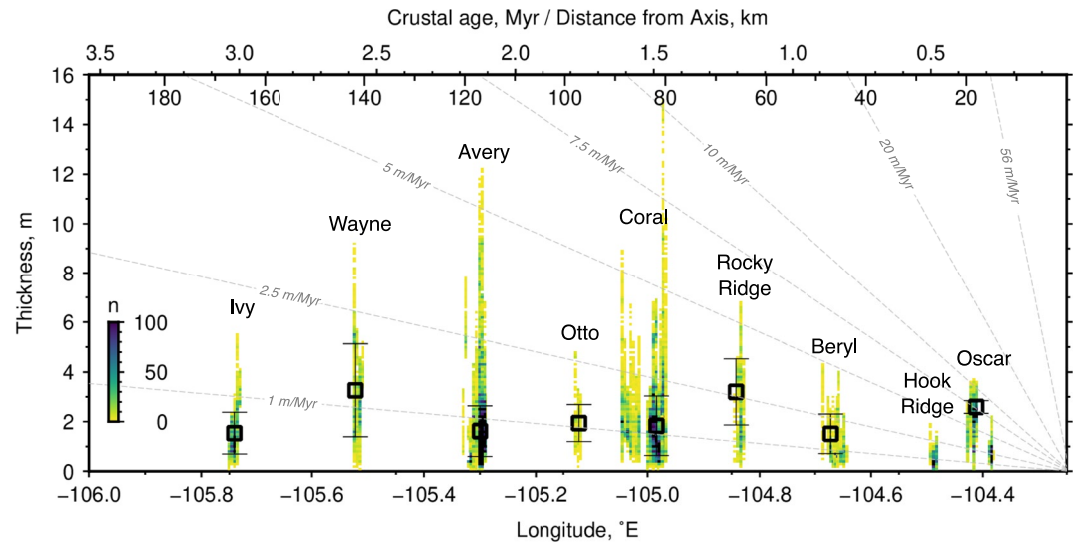


Figure 10. Sediment thickness versus longitude along 8°20'N seamount chain. Colors are binned sediment thickness estimates across entire seamount; black squares are mean sediment thickness at summits only; error bars are one standard deviation; dashed gray lines show predicted sediment thickness for a range of noted sedimentation rates; upper x-axis shows crustal age and distance from EPR axis assuming a full spreading rate of 107 mm/yr (Carbotte & Macdonald, 1992; DeMets et al., 2010).

reaching the thickest sediment cover of ~2.9 m on Coral's south flank. Further west, we observe a slight decrease in thickness at Avery (~1.6–2.1 m, Figures 9c–9e), but thicker sediment at Wayne seamount (~3 m; Figure 9b), and finally only ~1.5 m at the most distally located Ivy seamount (Figure 9a), although there is some variability in the position of these surveys with respect to the local seamount summits, which may bias the results.

4. Discussion

4.1. Nonlinear Off-Axis Volcanism Along the 8°20'N Seamount Chain

We observe a nonlinear relationship between nominal crustal age (inferred from a total spreading rate of 107 mm/yr and distance from the EPR axis), and the mean of summit sediment thickness (Figure 10). Although mass-wasting and sediment reworking by currents may have varying degrees of local influence, this pattern in sediment thickness can be used to infer the first order relative age of seafloor exposure and the relative timing of volcanic constructional phases between adjacent seamounts. For example, Coral seamount and Rocky Ridge (situated on the central portion of the chain, ~80 and 65 km from the EPR, respectively) have the thickest sedimentary cover: Coral's summit mean thickness is ~1.8 m, and mean overall thickness is 2.9 m with local basins containing up to ~15 m sediment; Rocky Ridge's summit mean thickness is ~3.2 m and mean overall thickness is ~2.5 m (see Figures 9i and 9j and 10). Hence, no recent volcanism is likely to have occurred to repave the sediment deposited on the summits of either of these seamounts. In contrast, Ivy seamount, at the distal end of the chain, has ~1.5 m of sediment at its summit, implying relatively recent volcanism, which is also supported by the visual observation of extinct hydrothermal chimneys during HOV *Alvin* dive 4848. Therefore, despite being situated on the oceanic crust that is 1.5 million years older, Ivy may have experienced volcanism more recently than Coral and Rocky Ridge. Similarly, Avery's southern flank and Wayne's summit (~120 and 140 km from the EPR axis, respectively) host sediments up to 12 and 9 m thick, respectively, based upon thickness estimates from CHIRP data and seafloor imagery (Figures 9b and 9e and 10). In order to test whether the apparently similar sediment thickness distributions for Ivy, Wayne, Avery, Coral, Beryl, and Oscar are part of a common group, we performed a one-way analysis of variance (ANOVA) test. We found that there was a statistically significant difference at the $p < 0.05$ level in mean sediment thickness between at least two seamounts ($F(5, 29,950) = 494$, $p = 0.01$). This result indicates that we can reject the null hypothesis and conclude that sediment thickness populations for these seamounts are unlikely to belong to a single group, supporting the notion that sedimentation is neither age-progressive, nor constant across the chain.

4.2. Limitations of Sediment Thickness Proxy

Sediment distribution is likely to be affected by several factors in addition to primary deposition as a function of seafloor exposure age. These factors include local seafloor relief (e.g., flat summits vs. steep slopes; see Figure 6 and Figure S1 in Supporting Information S1), changes in sedimentation rate, bottom currents (Figure 7, Figures S3, S4 and S5 in Supporting Information S1), and mass-wasting. Of these factors, strong bottom currents could play an important role in redistributing sediment (Xu et al., 2018). The shipboard ADCP data and HYCOM hindcast results are not sufficient to assess deep water circulation patterns affecting sediment mobility around the seamounts. The analysis of vehicle heading shows that current strength, at least at altitudes of 60–80 m above the seafloor, are generally weak except in local areas of Hook Ridge, Beryl, and Coral seamounts (*Sentry* dives 402, 406, and 521, respectively; see Figure 7, Figure S2 and Table S1 in Supporting Information S1). At these three locations, we find relatively thin sediment on the windward side of bathymetric highs and relatively thick sediments mainly concentrated on the flanks and local basin of the leeward side (Figures 5 and 6, and Figure S1 in Supporting Information S1). This non-uniform sediment distribution could be explained by westerly currents winnowing sediments from the windward bathymetric exposures and hence presents a potential bias in our use of sediment thickness as a proxy for exposure age. Thus, our interpretation of sediment thickness at Hook Ridge, Beryl, and Coral seamounts are tentative.

Flat-topped seamounts like Avery, Coral, Beryl, and Oscar have gently sloping summit plateaus, where sediment is least likely to be disturbed by mass-wasting and current activity. For example, the summits of Avery, Coral, Beryl, and Oscar have ~1.6, 1.8, 1.5, and 2.6 m of mean sediment thickness, respectively. Although mass-wasting and current activity may play a role on the flanks and basins around the seamounts, the relative amount of sediment cover on these summits agrees with the overall trends shown in Figures 5 and 6, and Figure S1 in Supporting Information S1. We expect that sediment thickness and its distribution is proportional to the exposure time of the seafloor and hence provide a tentative proxy for the relative timing of most recent volcanism. Since the sediment thickness does not linearly increase with crustal age along the 8°20'N seamount chain (assuming relatively constant sedimentation rates), individual constructs appear to have not erupted sequentially with increasing distance from the EPR. For instance, Coral and Wayne seamounts, located respectively at ~85 and ~140 km from the axis in the central area of the chain, yield the thickest mean sediment cover, and are likely to be the oldest volcanic constructs. An alternative interpretation proposes that Coral and Wayne have the oldest eruption history throughout the chain and the crust remained unchanged by any recent volcanic activity. The most distal seamount (Ivy, ~170 km away from the axis) has thinner sediment than the most proximal Oscar or Coral seamount. This difference indicates that despite being hosted on much older oceanic crust, the Ivy seamount likely experienced a magmatic episode more recently than constructs nearer to the axis.

Given the uncertainty in the timing of most recent volcanism at each seamount, absolute sedimentation rates (i.e., rather than relative seafloor exposure ages discussed above) inferred from our thickness estimates and nominal crustal ages, are likely to be inaccurate. Nonetheless, these estimates are mostly low, ranging between 1 and 2.5 m/Myr (Figure 10) for all but two seamounts in this study. Ivy seamount has the lowest apparent sedimentation rate at <1 m/Myr, while the highest rates of ~5–10 m/Myr are inferred at Oscar. These rates are considerably lower than the average sedimentation rate of 20 m/Myr inferred over the last ~150 ka from core INMD-14P (located at 8.80°N; 103.99°W), at 3,135 m water depth (Lyle et al., 2002) and 56 m/Myr over the past ~2.2 Myr inferred from seven sediment ponds (Sites 419 to 428) cored during Deep Sea Drilling Project (DSDP) Leg 54 (Rosendahl et al., 1980), located 55–141 km north from Coral seamount. This result is unsurprising since sedimentation rates on the bathymetric highs of the 8°20'N seamount chain are expected to be much less than that of the depositional lows targeted by DSDP Leg 54, where sediments are likely to be concentrated by deep-water current activity and mass-wasting. Our results underscore the importance of the local depositional environment and local currents when estimating sedimentation histories.

5. Conclusions

We find that sediment thickness on the summits of volcanic constructs across the 8°20'N seamount chain does not increase with distance from the EPR axis, suggesting that volcanism is not simply age-progressive along the seamount chain. We find that sediment is thickest in areas of low relief, such as flat-topped summits and local basins, likely due to the effects of gravitational mass-wasting. We use the deviation of AUV heading to estimate

current strength, which we find to be higher in places where sediments are thin or absent, such as on the summits of Coral and Beryl seamounts and at Hook Ridge, consistent with deep-water erosional current activity. At Ivy seamount, located ~170 km from the spreading center and located on oceanic crust nominally ~3 Myr in age, relatively thin sediment provides evidence for more recent volcanism than at other seamounts to the east, situated on younger oceanic crust. The nonlinear eruption history along the off-axis seamount chain suggests that magmatism varies in space and time, consistent with the geochemical variability observed in 8°20'N seamount lavas (Anderson et al., 2021). Our relative exposure age estimates, combined with highly variable basalt compositions (Anderson et al., 2021), suggest that off-axis volcanism along spreading-parallel seamount chains may be prolonged and episodic on the flanks of fast-spreading MORs. Therefore, independent plumbing systems and mantle sources are likely to be active with different melt upwelling histories. These findings suggest that the emplacement of seamounts and volcanic chains on the flanks of the EPR is not strictly related to the absolute plate motions. The tectonic evolution between the Siqueiros fracture zone and the ridge axis may have influenced the off-axis melt transport, and led to the formation of the 8°20'N seamounts.

Data Availability Statement

The shipboard multibeam bathymetry and autonomous underwater vehicle *Sentry* data presented here are available from the Marine Geoscience Data System, <https://doi.org/10.1594/IEDA/324043>; compressed high-intensity radiated pulse processing code is available at <https://doi.org/10.5281/zenodo.6463846> (Parnell-Turner, 2017). Figures were produced using the Generic Mapping Tools, v6 (Wessel et al., 2019).

Acknowledgments

We thank the Captain and crew of the R/V *Atlantis*, and the human-occupied vehicle *Alvin*, autonomous underwater vehicle *Sentry*, and shipboard scientific teams for their professionalism and hard work during cruises AT37-05 and AT42-06, and we thank G. Kurras for help in processing side-scan sonar imagery, and J.-N. Wu for advice in making figures. We are grateful for the thoughtful comments from two anonymous reviewers. This work was supported by National Science Foundation awards OCE-1356610, OCE-1356822, OCE-1357150, OCE-1754419, OCE-1834797, OCE-2001314, and OCE-20011331.

References

- Alexander, R. T., & Macdonald, K. C. (1996). Small off-axis volcanoes on the East Pacific Rise. *Earth and Planetary Science Letters*, 139(3–4), 387–394. [https://doi.org/10.1016/0012-821x\(96\)00028-3](https://doi.org/10.1016/0012-821x(96)00028-3)
- Allan, J. F., Batiza, R., & Lonsdale, P. (1987). Petrology and chemistry of lavas from seamounts flanking the East Pacific Rise axis, 21°N. *Implications concerning the mantle source composition for both seamount and adjacent EPR lavas. Seamounts, Islands, and Atolls, Geophysical Monograph Series*, 43, 255–282. <https://doi.org/10.1029/gm043p0255>
- Allan, J. F., Batiza, R., Perfit, M. R., Fornari, D. J., & Sack, R. O. (1989). Petrology of lavas from the Lamont seamount chain and adjacent East Pacific Rise, 10°N. *Journal of Petrology*, 30(5), 1245–1298. <https://doi.org/10.1093/petrology/30.5.1245>
- Anderson, M., Wanless, V. D., Perfit, M., Conrad, E., Gregg, P., Fornari, D., & Ridley, W. I. (2021). Extreme heterogeneity in mid-ocean ridge mantle revealed in lavas from the 8°20'N near-axis seamount chain. *Geochemistry, Geophysics, Geosystems*, 22(1), 1–22. <https://doi.org/10.1029/2020GC009322>
- Ballmer, M. D., Conrad, C. P., Smith, E. I., & Harmon, N. (2013). Non-hotspot volcano chains produced by migration of shear-driven upwelling toward the East Pacific Rise. *Geology*, 41(4), 479–482. <https://doi.org/10.1130/G33804.1>
- Batiza, R. (1982). Abundances, distribution, and sizes of volcanoes in the Pacific Ocean and implications for the origin of non-hotspot volcanoes. *Earth and Planetary Science Letters*, 60(2), 195–206. [https://doi.org/10.1016/0012-821x\(82\)90003-6](https://doi.org/10.1016/0012-821x(82)90003-6)
- Batiza, R., & Niu, Y. (1992). Petrology and magma chamber processes at the East Pacific Rise ~9°30'N. *Journal of Geophysical Research*, 97(B5), 6779–6797. <https://doi.org/10.1029/92JB00172>
- Batiza, R., & Vanko, D. (1984). Petrology of young Pacific seamounts. *Journal of Geophysical Research*, 89(B13), 11235–11260. <https://doi.org/10.1029/JB089iB13p11235>
- Behn, M. D., Lin, J., & Zuber, M. T. (2002). Evidence for weak oceanic transform faults. *Geophysical Research Letters*, 29(24), 1–4. <https://doi.org/10.1029/2002GL015162>
- Bleck, R., Rooth, C., Hu, D., & Smith, L. T. (1992). Ventilation patterns and mode water formation in a wind and thermodynamically driven isopycnic coordinate model of the North Atlantic. *Journal of Physical Oceanography*, 22(12), 1486–1505. [https://doi.org/10.1175/1520-0485\(1992\)022<1486:sdtia>2.0.co;2](https://doi.org/10.1175/1520-0485(1992)022<1486:sdtia>2.0.co;2)
- Brandl, P. A., Beier, C., Regelous, M., Abouchami, W., Haase, K. M., Garbe-Schönberg, D., & Galer, S. J. G. (2012). Volcanism on the flanks of the East Pacific Rise: Quantitative constraints on mantle heterogeneity and melting processes. *Chemical Geology*, 298–299, 41–56. <https://doi.org/10.1016/j.chemgeo.2011.12.015>
- Briais, A., Ondréas, H., Klingelhoefer, F., Dosso, L., Hamelin, C., & Guillou, H. (2009). Origin of volcanism on the flanks of the Pacific-Antarctic ridge between 41°30'S and 52°S. *Geochemistry, Geophysics, Geosystems*, 10(9). <https://doi.org/10.1029/2008GC002350>
- Cannat, M., Mangeny, A., Ondréas, H., Fouquet, Y., & Normand, A. (2013). High-resolution bathymetry reveals contrasting landslide activity shaping the walls of the Mid-Atlantic Ridge axial valley. *Geochemistry, Geophysics, Geosystems*, 14(4), 996–1011. <https://doi.org/10.1002/ggge.20056>
- Carbotte, S. M., & Macdonald, K. C. (1992). East Pacific Rise 8°–10°30'N: Evolution of ridge segments and discontinuities from SeaMARC II and three-dimensional magnetic studies. *Journal of Geophysical Research*, 97(B5), 6959–6982. <https://doi.org/10.1029/91jb03065>
- Carbotte, S. M., Marjanović, M., Carton, H., Mutter, J. C., Canales, J. P., Nedimovi, M. R., et al. (2013). Fine-scale segmentation of the crustal magma reservoir beneath the East Pacific Rise. *Nature Geoscience*, 6(10), 866–870. <https://doi.org/10.1038/ngeo1933>
- Carrass, D. W., & Chayes, D. L. (1996). Improved processing of hydroswEEP DS multibeam data on the R/V *Maurice Ewing*. *Marine Geophysical Researches*, 18(6), 631–650. <https://doi.org/10.1007/bf00313878>
- Choi, H., Kim, S. S., & Park, S. H. (2021). Magnetic constraints on off-axis seamount volcanism in the easternmost segment of the Australian-Antarctic ridge. *Geochemistry, Geophysics, Geosystems*, 22(9), 1–18. <https://doi.org/10.1029/2020GC009576>
- Christeson, G. L., Goff, J. A., & Reece, R. S. (2019). Synthesis of oceanic crustal structure from two-dimensional seismic profiles. *Reviews of Geophysics*, 57(2), 504–529. <https://doi.org/10.1029/2019RG000641>

- Clague, D. A., Reynolds, J. R., & Davis, A. S. (2000). Near-ridge seamount chains in the northeastern Pacific Ocean. *Journal of Geophysical Research*, *105*(B7), 16541–16561. <https://doi.org/10.1029/2000jb900082>
- Clouard, V., & Bonneville, A. (2005). Ages of seamounts, islands and plateaus on the Pacific plate. *Geological Society of America Special Paper*, *388*, 71–90.
- Cohen, J. K., & Stockwell, J. W. (2013). *CWP/SU: Seismic Unix. Release No. 43R5: An open source software package for seismic research and processing*. Center for Wave Phenomena, Colorado School of Mines.
- Coumans, J. P., Stix, J., Clague, D. A., & Minarik, W. G. (2014). The magmatic architecture of Taney seamount-A, NE Pacific Ocean. *Journal of Petrology*, *56*(6), 1037–1067. <https://doi.org/10.1093/petrology/egv027>
- Crane, K. (1976). The intersection of the Siqueiros transform fault and the East Pacific Rise. *Marine Geology*, *21*(1), 25–46. [https://doi.org/10.1016/0025-3227\(76\)90102-X](https://doi.org/10.1016/0025-3227(76)90102-X)
- Davis, A. S., & Clague, D. A. (2000). President Jackson seamounts, northern Gorda ridge: Tectonomagmatic relationship between on- and off-axis volcanism. *Journal of Geophysical Research*, *105*(B12), 27939–27956. <https://doi.org/10.1029/2000jb900291>
- Davis, E. E., & Karsten, J. L. (1986). On the cause of the asymmetric distribution of seamounts about the Juan de Fuca ridge: Ridge-crest migration over a heterogeneous asthenosphere. *Earth and Planetary Science Letters*, *79*(3–4), 385–396. [https://doi.org/10.1016/0012-821X\(86\)90194-9](https://doi.org/10.1016/0012-821X(86)90194-9)
- DeMets, C., Gordon, R. G., & Argus, D. F. (2010). Geologically current plate motions. *Geophysical Journal International*, *181*(1), 1–80. <https://doi.org/10.1111/j.1365-246X.2009.04491.x>
- Edwards, M. H., Fornari, D. J., Malinverno, A., Ryan, W. B. F., & Madsen, J. A. (1991). The regional tectonic fabric of the East Pacific Rise from 12°50'N to 15°10'N. *Journal of Geophysical Research*, *96*(B5), 7995–8018. <https://doi.org/10.1029/91jb00283>
- Fornari, D. J., Gallo, D. G., Edwards, M. H., Madsen, J. A., Perfit, M. R., & Shor, A. N. (1989). Structure and topography of the Siqueiros transform fault system: Evidence for the development of intra-transform spreading centers. *Marine Geophysical Researches*, *11*(4), 263–299. <https://doi.org/10.1007/BF00282579>
- Fornari, D. J., Perfit, M. R., Allan, J. F., & Batiza, R. (1988). Small-scale heterogeneities in depleted mantle sources: Near-ridge seamount lava geochemistry and implications for mid-ocean-ridge magmatic processes. *Nature*, *331*(6156), 511–513. <https://doi.org/10.1038/331511a0>
- Fornari, D. J., Perfit, M. R., Allan, J. F., Batiza, R., Haymon, R., Barone, A., et al. (1988). Geochemical and structural studies of the Lamont seamounts: Seamounts as indicators of mantle processes. *Earth and Planetary Science Letters*, *89*(1), 63–67. [https://doi.org/10.1016/0012-821X\(88\)90033-7](https://doi.org/10.1016/0012-821X(88)90033-7)
- Fox, P. J., & Gallo, D. G. (1984). A tectonic model for ridge-transform-ridge plate boundaries: Implications for the structure of oceanic lithosphere. *Tectonophysics*, *104*(3–4), 205–242. [https://doi.org/10.1016/0040-1951\(84\)90124-0](https://doi.org/10.1016/0040-1951(84)90124-0)
- Goff, J. A. (1991). A global and regional stochastic analysis of near-ridge abyssal hill morphology. *Journal of Geophysical Research*, *96*(B13), 21713–21737. <https://doi.org/10.1029/91jb02275>
- Gregg, P. M., Behn, M. D., Lin, J., & Grove, T. L. (2009). Melt generation, crystallization, and extraction beneath segmented oceanic transform faults. *Journal of Geophysical Research*, *114*(11), 1–16. <https://doi.org/10.1029/2008JB006100>
- Halliwel, G. R., Bleck, R., & Chassignet, E. (1998). *Atlantic Ocean simulations performed using a new hybrid-coordinate ocean model*. EOS, Fall 1998 AGU Meeting.
- Halliwel, G. R., Bleck, R., Chassignet, E. P., & Smith, L. T. (2000). Mixed layer model validation in Atlantic Ocean simulations using the hybrid coordinate ocean model (HYCOM). *EOS*, *80*(OS304).
- Harmon, R. M., Forsyth, D. W., Weeraratne, D. S., Yang, Y., & Webb, S. C. (2011). Mantle heterogeneity and off-axis volcanism on young Pacific lithosphere. *Earth and Planetary Science Letters*, *311*(3–4), 306–315. <https://doi.org/10.1016/j.epsl.2011.09.038>
- Harms, J. C. (1969). Hydraulic significance of some sand ripples. *Geological Society of America Bulletin*, *80*(3), 363. [https://doi.org/10.1130/0016-7606\(1969\)80\[363:HSOSSR\]2.0.CO;2](https://doi.org/10.1130/0016-7606(1969)80[363:HSOSSR]2.0.CO;2)
- Haymon, R. M., Fornari, D. J., Edwards, M. H., Carbotte, S., Wright, D., & Macdonald, K. C. (1991). Hydrothermal vent distribution along the East Pacific Rise crest (9°09'–54'N) and its relationship to magmatic and tectonic processes on fast-spreading mid-ocean ridges. *Earth and Planetary Science Letters*, *104*(2–4), 513–534. [https://doi.org/10.1016/0012-821X\(91\)90226-8](https://doi.org/10.1016/0012-821X(91)90226-8)
- Hebert, L. B., & Montési, L. G. J. (2011). Melt extraction pathways at segmented oceanic ridges: Application to the East Pacific Rise at the Siqueiros transform. *Geophysical Research Letters*, *38*(11), 1–5. <https://doi.org/10.1029/2011GL047206>
- Hillier, J. K., & Watts, A. B. (2007). Global distribution of seamounts from ship-track bathymetry data. *Geophysical Research Letters*, *34*(13), 1–5. <https://doi.org/10.1029/2007GL029874>
- Hwang, G., & Kim, S. S. (2016). Flexure and gravity anomalies of the oceanic lithosphere beneath the Louisville seamount. *Tectonophysics*, *686*, 19–26. <https://doi.org/10.1016/j.tecto.2016.07.014>
- Johnson, G. C., & Toole, J. M. (1993). Flow of deep and bottom waters in the Pacific at 10°N. *Deep Sea Research Part I: Oceanographic Research Papers*, *40*(2), 371–394. [https://doi.org/10.1016/0967-0637\(93\)90009-R](https://doi.org/10.1016/0967-0637(93)90009-R)
- Katz, R. F., Spiegelman, M., & Holtzman, B. (2006). The dynamics of melt and shear localization in partially molten aggregates. *Nature*, *442*(7103), 676–679. <https://doi.org/10.1038/nature05039>
- Klein, E. M., White, S. M., Nunnery, J. A., Mason-Stack, J. L., Wanless, V. D., Perfit, M. R., et al. (2013). Seafloor photo-geology and sonar terrain modeling at the 9°N overlapping spreading center, East Pacific Rise. *Geochemistry, Geophysics, Geosystems*, *14*(12), 5146–5170. <https://doi.org/10.1002/2013GC004858>
- Koppers, A. A. P., Steinberger, B., & Duncan, R. A. (2004). Implications of a nonlinear ⁴⁰Ar/³⁹Ar age progression along the Louisville seamount trail for models of fixed and moving hot spots. *Geochemistry, Geophysics, Geosystems*, *5*(6), 1–22. <https://doi.org/10.1029/2003GC000671>
- Koppers, A. A. P., Yamazaki, T., Geldmacher, J., Gee, J. S., Pressling, N., Hoshi, H., et al. (2012). Limited latitudinal mantle plume motion for the Louisville hotspot. *Nature Geoscience*, *5*(12), 911–917. <https://doi.org/10.1038/ngeo1638>
- Kunze, E., Firing, E., Hummon, J. M., Chereskin, T. K., & Thurnherr, A. M. (2006). Global abyssal mixing inferred from lowered ADCP shear and CTD strain profiles. *Journal of Physical Oceanography*, *36*(8), 1553–1576. <https://doi.org/10.1175/jpo2926.1>
- Langmuir, C. H., Bender, J. F., & Batiza, R. (1986). Petrological and tectonic segmentation of the East Pacific Rise, 5°30'–14°30' N. *Nature*, *322*(6078), 422–429. <https://doi.org/10.1038/322422a0>
- Langmuir, C. H., Klein, E., & Plank, T. (1992). Petrological Systematics of Mid-Ocean Ridge Basalts: Constraints on Melt Generation Beneath Ocean Ridges, in *Mantle Flow and Melt Generation at Mid-Ocean Ridges*. *Geophysical Monograph, American Geophysical Union*, *71*, 183–280. <https://doi.org/10.1029/gm071p0183>
- Lavelle, J. W., & Mohn, C. (2010). Motion, commotion, and biophysical connections at deep ocean seamounts. *Oceanography*, *23*(1), 90–103. <https://doi.org/10.5670/oceanog.2010.64>
- Lonsdale, P. (1993). Overlapping rift zones at the 5.5°S offset of the East Pacific Rise. *Journal of Geophysical Research*, *88*, 9393–9406. <https://doi.org/10.1029/JB088iB11p09393>

- Lonsdale, P., & Spiess, F. N. (1977). Abyssal bedforms explored with a deeply towed instrument package. *Developments in Sedimentology*, 23, 57–75. [https://doi.org/10.1016/S0070-4571\(08\)70550-8](https://doi.org/10.1016/S0070-4571(08)70550-8)
- Lyle, M., Mix, A., & Pisias, N. (2002). Patterns of CaCO₃ deposition in the eastern tropical Pacific Ocean for the last 150 kyr: Evidence for a south-east Pacific depositional spike during marine isotope stage (MIS) 2. *Paleoceanography*, 17(2), 3–1–3–13. <https://doi.org/10.1029/2000pa000538>
- Macdonald, K. C., Fox, P. J., Miller, S., Carbotte, S., Edwards, M. H., Eisen, M., et al. (1992). The East Pacific Rise and its flanks 8–18°N: History of segmentation, propagation and spreading direction based on SeaMARC II and Sea Beam studies. *Marine Geophysical Researches*, 14(4), 299–344. <https://doi.org/10.1007/BF01203621>
- Macdonald, K. C., Fox, P. J., Perram, L. J., Eisen, M. F., Haymon, R. M., Miller, S. P., et al. (1988). A new view of the mid-ocean ridge from the behaviour of ridge-axis discontinuities. *Nature*, 335(6187), 217–225. <https://doi.org/10.1038/335217a0>
- Mantyla, A. W. (1975). On the potential temperature in the abyssal Pacific Ocean. *Journal of Marine Research*, 33(1975), 341–354.
- Niu, Y., & Batiza, R. (1997). Trace element evidence from seamounts for recycled oceanic crust in the Eastern Pacific mantle. *Earth and Planetary Science Letters*, 148(3–4), 471–483. [https://doi.org/10.1016/s0012-821x\(97\)00048-4](https://doi.org/10.1016/s0012-821x(97)00048-4)
- Parnell-Turner, R. (2017). *auv-chirp*. GitHub Repository. Retrieved from <https://github.com/Rparnellturner/Auv-Chirp>
- Perfit, M. R., Fornari, D. J., Ridley, W. I., Kirk, P. D., Casey, J., Kastens, K. A., et al. (1996). Recent volcanism in the Siqueiros transform fault: Picritic basalts and implications for MORB magma genesis. *Earth and Planetary Science Letters*, 141(1–4), 91–108. [https://doi.org/10.1016/0012-821x\(96\)00052-0](https://doi.org/10.1016/0012-821x(96)00052-0)
- Perfit, M. R., Fornari, D. J., Smith, M. C., Bender, J. F., Langmuir, C. H., & Haymon, R. M. (1994). Small-scale spatial and temporal variations in mid-ocean ridge crest magmatic processes. *Geology*, 22(4), 375–379. [https://doi.org/10.1130/0091-7613\(1994\)022<0375:SSATV>2.3.CO;2](https://doi.org/10.1130/0091-7613(1994)022<0375:SSATV>2.3.CO;2)
- Pockalny, R. A., Fox, P. J., Fornari, D. J., Macdonald, K. C., & Perfit, M. R. (1997). Tectonic reconstruction of the Clipperton and Siqueiros fracture zones: Evidence and consequences of plate motion change for the last 3 Myr. *Journal of Geophysical Research*, 102(B2), 3167–3181. <https://doi.org/10.1029/96jb03391>
- Polzin, K. L., Toole, J. M., Ledwell, J. R., & Schmitt, R. W. (1997). Spatial variability of turbulent mixing in the abyssal ocean. *Science*, 276(5309), 93–96. <https://doi.org/10.1126/science.276.5309.93>
- Reynolds, J. R., & Langmuir, C. H. (2000). Identification and implications of off-axis lava flows around the East Pacific Rise. *Geochemistry, Geophysics, Geosystems*, 1(6). <https://doi.org/10.1029/1999GC000033>
- Romano, V., Gregg, P., Zhan, Y., Fornari, D., Perfit, M., & Battaglia, M. (2017). *Formation and evolution of the near axis 8°20'N seamount chain: Evidences from the geophysical data analysis*. Abstract V51D0391 presented at American Geophysical Union Fall Meeting, Dec. 11–15.
- Rosendahl, B. R., Hekinian, R., Briquieu, L., Dmitriev, Y., Fodor, R. V., Goll, R. M., et al. (1980). *Initial reports of the Deep Sea drilling Project*, v. 54. Washington (U.S. Government Printing Office).
- Scheirer, D. S., & Macdonald, K. C. (1995). Near-axis seamounts on the flanks of the East Pacific Rise, 8°N to 17°N. *Journal of Geophysical Research*, 100(B2), 2239–2259. <https://doi.org/10.1029/94JB02769>
- Seton, M., Müller, R. D., Zahirovic, S., Williams, S., Wright, N. M., Cannon, J., et al. (2020). A global data set of present-day oceanic crustal age and seafloor spreading parameters. *Geochemistry, Geophysics, Geosystems*, 21(10), 1–15. <https://doi.org/10.1029/2020GC009214>
- Smith, D. K. (1988). Shape analysis of Pacific seamounts. *Earth and Planetary Science Letters*, 90(4), 457–466. [https://doi.org/10.1016/0012-821X\(88\)90143-4](https://doi.org/10.1016/0012-821X(88)90143-4)
- Smith, D. K., & Cann, J. R. (1992). The role of seamount volcanism in crustal construction at the Mid-Atlantic Ridge (24°–30°N). *Journal of Geophysical Research*, 97(B2), 1645–1658. <https://doi.org/10.1029/91jb02507>
- Sohn, R. A., & Sims, K. W. W. (2005). Bending as a mechanism for triggering off-axis volcanism on the East Pacific Rise. *Geology*, 33(2), 93–96. <https://doi.org/10.1130/G21116.1>
- Thurnherr, A. M., Ledwell, J. R., Lavelle, J. W., & Mullineaux, L. S. (2011). Hydrography and circulation near the crest of the East Pacific Rise between 9° and 10°N. *Deep-Sea Research Part I: Oceanographic Research Papers*, 58(4), 365–376. <https://doi.org/10.1016/j.dsr.2011.01.009>
- Thurnherr, A. M., & St. Laurent, L. C. (2011). Turbulence and diapycnal mixing over the East Pacific Rise crest near 10°N. *Geophysical Research Letters*, 38(15), 2–5. <https://doi.org/10.1029/2011GL048207>
- Toomey, D. R., Jousset, D., Dunn, R. A., Wilcock, W. S. D., & Detrick, R. S. (2007). Skew of mantle upwelling beneath the East Pacific Rise governs segmentation. *Nature*, 446(7134), 409–414. <https://doi.org/10.1038/nature05679>
- Tsuchiya, M., & Talley, L. D. (1998). A Pacific hydrographic section at 88°W: Water-property distribution. *Journal of Geophysical Research*, 103(C6), 12899–12918. <https://doi.org/10.1029/97JC03415>
- Turnewitsch, R., Falahat, S., Nycander, J., Dale, A., Scott, R. B., & Furnival, D. (2013). Deep-sea fluid and sediment dynamics-Influence of hill-to seamount-scale seafloor topography. *Earth-Science Reviews*, 127, 203–241. <https://doi.org/10.1016/j.earscirev.2013.10.005>
- Wanless, V., & Shaw, A. (2012). Lower crustal crystallization and melt evolution at mid-ocean ridges. *Nature Geoscience*, 5(9), 651–655. <https://doi.org/10.1038/ngeo1552>
- Waters, C. L., Sims, K. W. W., Klein, E. M., White, S. M., Reagan, M. K., & Girard, G. (2013). Sill to surface: Linking young off-axis volcanism with subsurface melt at the overlapping spreading center at 9°03'N East Pacific Rise. *Earth and Planetary Science Letters*, 369–370, 59–70. <https://doi.org/10.1016/j.epsl.2013.03.006>
- Watts, A. B., Sandwell, D. T., Smith, W. H. F., & Wessel, P. (2006). Global gravity, bathymetry, and the distribution of submarine volcanism through space and time. *Journal of Geophysical Research*, 111(B8), 1–26. <https://doi.org/10.1029/2005JB004083>
- Watts, A. B., Weisell, J. K., Duncan, R. A., & Larson, R. L. (1988). Origin of the Louisville Ridge and its relationship to the Eltanin fracture zone system. *Journal of Geophysical Research*, 93(B4), 3051–3077. <https://doi.org/10.1029/JB093iB04p03051>
- Wessel, P., Luis, J. F., Uieda, L., Scharroo, R., Wobbe, F., Smith, W. H. F., & Tian, D. (2019). The Generic Mapping Tools Version 6. *Geochemistry, Geophysics, Geosystems*, 20(11), 5556–5564. <https://doi.org/10.1029/2019gc008515>
- White, S. M., Haymon, R. M., & Carbotte, S. (2006a). A new view of ridge segmentation and near-axis volcanism at the East Pacific Rise, 8°–12°N, from EM300 multibeam bathymetry. *Geochemistry, Geophysics, Geosystems*, 7(12). <https://doi.org/10.1029/2006GC001407>
- White, S. M., Macdonald, K. C., Scheirer, S., & Cormier, M. H. (1998). Distribution of isolated volcanoes on the flanks of the East Pacific Rise, 15.3°S–20°S. *Journal of Geophysical Research*, 103(B12), 30371–30384. <https://doi.org/10.1029/98jb02791>
- White, S. M., Mason, J. L., Macdonald, K. C., Perfit, M. R., Wanless, V. D., & Klein, E. M. (2009). Significance of widespread low effusion rate eruptions over the past two million years for delivery of magma to the overlapping spreading centers at 9°N East Pacific Rise. *Earth and Planetary Science Letters*, 280(1–4), 175–184. <https://doi.org/10.1016/j.epsl.2009.01.030>
- White, S. M., Umino, S., & Kumagai, H. (2006b). Transition from seamount chain to intraplate volcanic ridge at the East Pacific Rise. *Geology*, 34(4), 293–296. <https://doi.org/10.1130/G2234.1>
- Xu, G., McGillicuddy, D. J., Mills, S. W., & Mullineaux, L. S. (2018). Dispersal of hydrothermal vent Larvae at East Pacific Rise 9–10°N segment. *Journal of Geophysical Research: Oceans*, 123(11), 7877–7895. <https://doi.org/10.1029/2018JC014290>